UC Santa Cruz
UC Santa Cruz Previously Published Works

Title
Giant energy storage and power density negative capacitance superlattices

Permalink
https://escholarship.org/uc/item/9v13j8fx

Journal
Nature, 629(8013)

ISSN
0028-0836

Authors
Cheema, Suraj S
Shanker, Nirmaan
Hsu, Shang-Lin
et al.

Publication Date
2024-05-23

DOI
10.1038/s41586-024-07365-5

Copyright Information
This work is made available under the terms of a Creative Commons Attribution-NonCommercial-NoDerivatives License, available at
https://creativecommons.org/licenses/by-nc-nd/4.0/

Peer reviewed

eScholarship.org Powered by the California Digital Library
University of California

Giant energy storage ultrafast microcapacitors via negative capacitance superlattices

Suraj S. Cheema,[1*†] Nirmaan Shanker,[1†] Shang-Lin Hsu,[1†] Joseph Schaadt,[1,2] Nathan M. Ellis,[1] Matthew Cook,[3] Ravi Rastogi,[3] Robert C.N. Pilawa-Podgurski,[1] Jim Ciston,[4] Mohamed Mohamed,[3] Sayeef Salahuddin[1,5*]

[1]*Department of Electrical Engineering and Computer Sciences, University of California, Berkeley, CA, USA.*

[2]*Department of Mechanical Engineering, University of California, Berkeley, CA, USA.*

[3]*Lincoln Laboratory, Massachusetts Institute of Technology, Lexington, MA, USA.*

[4]*National Center for Electron Microscopy Facility, Molecular Foundry, Lawrence Berkeley National Laboratory, Berkeley, CA, USA.*

[5]*Materials Sciences Division, Lawrence Berkeley National Laboratory, Berkeley, CA, USA.*

[†]***These authors contributed equally to this work.***

[*]***Correspondence to: s.cheema@berkeley.edu (S.S.C), sayeef@berkeley.edu (S.S.)***

Dielectric electrostatic capacitors[1], due to their ultrafast charge-discharge capability, are attractive for high power energy storage applications. Along with ultrafast operation, on-chip integration can enable miniaturized energy storage devices for emerging autonomous microelectronics and microsystems[2–6]. Additionally, state-of-the-art miniaturized electrochemical energy storage systems – microsupercapacitors and microbatteries – currently face safety, packaging, materials, and microfabrication challenges preventing on-chip technological readiness[2–5,7,8], leaving an opportunity for electrostatic microcapacitors. Here we report record-high energy storage density (ESD) and power density (PD) across all electrostatic systems in HfO_2-ZrO_2 (HZO)-based thin film microcapacitors integrated directly on silicon, through a three-pronged approach. First, to increase intrinsic energy storage, atomic-layer-deposited antiferroelectric HZO films are engineered near a field-driven ferroelectric phase transition to exhibit amplified charge storage via the negative capacitance (NC) effect[9–15], which enhances volumetric-ESD beyond the best-known back-end-of-the-line (BEOL) compatible dielectrics (115 J-cm^{-3})[16]. Second, to increase overall stored energy, antiferroelectric superlattice engineering[17,18] ~~of amorphous-templated HZO-Al_2O_3 heterostructures~~ scales-up the ~~high-storage antiferroelectric-NC behavior~~ energy storage performance to the 100-nm regime, which overcomes the conventional thickness limitations of HZO-based (anti)ferroelectricity ~~(10-nm regime)~~[19]. Third, to increase storage-per-footprint, the superlattices are conformally integrated into three-dimensional (3D) capacitors, which boosts areal-ESD (areal-PD) 9-times (170-times) the best-known 3D electrostatic capacitors: 80 mJ-cm^{-2} (300 kW-cm^{-2}). This simultaneous demonstration of ultrahigh ESD and PD overcomes the traditional capacity-speed trade-off across the electrostatic-electrochemical energy storage hierarchy[1]. Furthermore, integration of ultrahigh-density and ultrafast-charging thin films within a BEOL-compatible process enables monolithic integration[20] of on-chip microcapacitors, which opens the door for substantial energy storage and power delivery for electronic microsystems.

Main Dielectric electrostatic capacitors have emerged as ultrafast charge-discharge sources boasting ultrahigh power densities relative to their electrochemical counterparts[1]. However, electrostatic capacitors lag behind in energy storage density (ESD) compared to electrochemical paradigms[1,21]. To close this gap, dielectrics could amplify their energy storage per unit planar area if packed into scaled three-dimensional (3D) structures[2]. Such 3D microcapacitor integration on silicon would mark a breakthrough for realizing miniaturized on-chip energy storage towards more sustainable and autonomous electronic microsystems[2–5].

Thus far, the highest energy storage dielectrics are complex oxide nonlinear dielectrics, particularly epitaxial relaxor-like ferroelectrics[22–24]. These systems have negligible remnant polarization (P_r) – leading to low energy loss – and ultrahigh polarizability relative to other prototypical ferroelectric material systems – leading to large dielectric response under electric fields. However, the need for epitaxial substrates and high temperature synthesis pose major challenges for scaling and integrating these material systems[16].

The discovery of ferroelectricity and antiferroelectricity in simple HfO_2- and ZrO_2-based thin films[19] overcomes many of the thickness scaling[25] and compatibility[26] challenges facing its complex oxide nonlinear dielectric counterparts. In these simple binary oxides, (anti)ferroelectric order can be stabilized at low thermal budget[27] – below the 400°C requirement for BEOL compatibility – down to the ultrathin limit on Si[28,29] via atomic layer deposition (ALD)[30]. Critically, ALD fosters wafer-scale conformal growth into highly-scaled 3D structures not possible with other functional oxide thin film deposition techniques[30]. Indeed, HfO_2- and ZrO_2-based thin films have replaced SiO_2 as the dielectric layer in mass production microelectronic devices[31]. Until now, the promise of ultrathin (anti)ferroelectricity on Si has mostly motivated low-power computing applications[32–34]. Due to shared underlying traits, the same features which make HfO_2-ZrO_2 so promising for computing – (anti)ferroelectric order down to the ultrathin regime[14,28,29,35–37], high permittivity (κ) via ferroic phase engineering[14,38], ferroic phase transitions[39,40] and polymorphs[41], inherently large breakdown field and bandgap[31], conformal growth by ALD[30] – are also appealing for energy storage applications[16,42,43].

Despite these attractive materials- and integration-level characteristics, HfO_2- and ZrO_2-

based binary oxides historically lag behind their complex oxide dielectric counterparts in two key energy storage metrics. First, the top-performing complex perovskite-structure oxides boast much larger volumetric ESD ($>$ 100 J/cm^3)[22–24] than fluorite-structure binary oxides ($\sim$ 40-70 J/cm^3)[16] (Supplementary Table 1). Second, fluorite-structure thin films struggle to maintain their highly-polarizable (anti)ferroelectric crystal structures past the 10 nm thickness regime; this size-effect restriction prevents scaling up their total energy storage linearly with thickness[44] (Supplementary Table 1).

To address these limitations, this work not only overcomes both intrinsic issues plaguing fluorite-structure binary oxides – energy storage capability and thickness scaling – but also integrates the optimized HfO_2-ZrO_2 (HZO) system into 3D Si capacitors to further enhance its total energy storage, through a three step approach (Extended Data Fig. 1). First, the intrinsic charge storage ability in the HZO system is optimized through ferroic phase engineering and the ~~antiferroelectric~~ field-driven negative capacitance (NC) effect, resulting in larger ESD than the best-known BEOL-compatible dielectrics ($>$ 100 J/cm^3). Next, amorphous-templated superlattices help the high-κ HZO ~~antiferroelectric~~ field-driven NC behavior to persist to two-times the thickest value reported for ALD-grown HfO_2- or ZrO_2-based (anti)ferroelectrics ($\sim$ 100 nm), enabling the ideal antiferroelectric NC energy storage behavior to scale up. Finally, we leverage the microelectronics maturity of the HZO system – integration into 3D Si trench structures used in current semiconductor technology – to increase the energy storage per footprint (> 100x boost). Ultimately, the ferroic-engineered NC HZO superlattice films integrated into 3D Si capacitors demonstrate record energy storage (80 mJ/cm^2) and power density (300 kW/cm^2) across all dielectric electrostatic capacitors. These results mark a breakthrough towards realizing on-chip energy storage with both ultrahigh capacity and ultrafast operation.

Ultrahigh energy storage via antiferroelectric negative capacitance To first optimize the intrinsic energy storage capability in the fluorite-structure family, the HfO_2-ZrO_2 (HZO) dielectric phase space is considered for ALD-grown 9-nm HZO films on TiN-buffered Si (Methods). Capacitance-voltage (C-V) measurements across the composition phase space (Fig. 1a,b) illustrate the expected evolution from the ferroelectric orthorhombic phase (o-phase: $Pca2_1$) at intermediate

Zr-content to the antiferroelectric tetragonal phase (t-phase; $P4_2/nmc$) at large Zr-content[19]. In particular, our approach looks to engineer the fluorite-structure antiferroelectric phase, in which the parent non-polar t-phase transforms into the polar o-phase upon the application of an electric field[40]. At this field-driven ferroic phase transition, there exists a super-linear charge response (denoted Regime II) identified from pulsed charge-voltage (*Q*-*V*) measurements (Fig. 1c, Extended Data Fig. 2). This super-linear Regime II increases the energy storage capacity, calculated from integrating hysteretic charge-discharge *Q*-*V* loops (Fig. 1d, Extended Data Fig. 2, Methods).

Investigation of the energy density as a function of composition (Fig. 1e) shows that there is a peak in the volumetric energy storage (115 J/cm^3) at 80% Zr content, which corresponds to the squeezed antiferroelectric state from *C*-*V* loops (Fig. 1b). The squeezed antiferroelectric state refers to a lower critical field for the antiferroelectric-to-ferroelectric phase transition in comparison to the normal antiferroelectric state observed for 100% Zr content, as previously observed for doped ZrO_2[45,46]. In the normal antiferroelectric state, the onset of the desirable super-linear Regime II (Fig 1c,d) is delayed, so the film cannot reap the enhanced energy storage benefits across as wide a voltage window as the squeezed antiferroelectric state before breakdown. Upon further lowering the ZrO_2 content below the optimal composition (80%), the ESD decreases because the starting phase fraction is partially ferroelectric i.e. a mixed ferroelectric-antiferroelectric state. In the mixed ferroic state, the initial ferroelectric phase fraction decreases the electric field window of the super-linear Regime II, in which the antiferroelectric t-phase converts to the ferroelectric o-phase, thereby lowering the total possible charge stored upon integration. Thus, to obtain high energy density, the width of the super-linear Regime II was maximized to take advantage of the enhanced charge response present in Regime II.

To further understand the origin of this super-linear Regime II leading to ultrahigh energy density, examination of the hysteretic *Q*-*V* loop demonstrates the presence of a negative *dQ/dV* slope, i.e. negative capacitance (NC), at intermediate fields (Fig. 1f, Methods), which was first observed during polarization switching in perovskite ferroelectrics[47]. NC was first proposed[9] and demonstrated[10] in ferroelectric-dielectric systems to benefit low-power computing applications, but the same underlying principle – enhanced capacitance i.e. charge storage at a given voltage –

is also promising for energy storage. Indeed, the traditional ferroelectric-dielectric picture of NC was previously explored for enhancing electrostatic energy storage in HZO[48]. Here, we consider exploiting a different mechanism of NC – ~~antiferroelectric~~ field-driven NC – to generate boosted charge for enhanced energy storage. NC has been recently demonstrated in fluorite-structure antiferroelectric ZrO_2[49] and canonical perovskite-structure antiferroelectric $PbZrO_3$[50]. In particular, the structural origin of NC in both fluorite-structure and perovskite-structure antiferroelectrics has been linked to a field-induced phase transition from a nonpolar antiferroelectric phase to a polar ferroelectric phase[49,50].

The ~~antiferroelectric~~ field-driven NC picture can be understood through the energy landscape evolution for antiferroelectric HZO at different electric fields (~~Fig. 1g~~ Supplementary Fig. 1a). Spanning low-field Regime I (native antiferroelectric t-phase), intermediate-field Regime II (mixed antiferroelectric-ferroelectric co-existence), and high-field Regime III (fully converted ferroelectric o-phase), we observe the net system is stabilized in its negative curvature portion of the energy landscape – i.e. negative capacitance state – during Regime II. Engineering competing nonpolar-polar structures – dielectric-ferroelectric[10,12] or antiferroelectric-ferroelectric[14] – underlies NC stabilization as depolarizing fields from the nonpolar region can counteract the polar ferroelectric region and help stabilize the negative curvature portion of the energy landscape (Supplementary Fig. 1a) as demonstrated in original NC experimental demonstrations[10–12,14]. While the external electric field may overcome the depolarization fields originating from electrostatic coupling of the nonpolar antiferroelectric and polar ferroelectric phases, the enhanced prevalence of domain walls[11,12] and local heterogeneity[51] due to the coexistence of nonpolar and polar grains in Regime II can still induce effective depolarization fields and flatten the energy landscape[11,12,51]. For example, heterogeneous elastic energies in structurally inhomogeneous systems have been shown to destabilize long-range polarization, suppress polarization, and thereby flatten energy landscapes[51]. Moreover, competing antiferroelectric-ferroelectric phases in HfO_2-ZrO_2 have led to NC and enhanced charge response in its ground state[14]. ~~In this case, field-induced NC stabilization from competing antiferroelectric-ferroelectric structures~~ In contrast to past NC work stabilizing the mixed antiferroelectric-ferroelectric phases in HfO_2-ZrO_2 without an applied field[14], here

we stabilize the same competing antiferroelectric-ferroelectric phases under the application of an applied field to stabilize NC, leading to amplified charge and energy storage in Regime II rather than its ground state, resulting in record-setting volumetric energy density for a BEOL-compatible dielectric (115 J/cm^3, Supplementary Table 1). Ultimately, the antiferroelectric field-driven phase transition and the resulting highly polarizable dielectric medium serves as the underlying origin of the change in slope and enhanced energy storage performance in Regime II; furthermore, the correlation between the -dQ/dV region and the enhanced energy density slope region in Regime II strongly indicates the presence of NC during the phase transition.

Scaling up total energy storage via antiferroelectric superlattices Although the 9 nm HZO films demonstrate record recoverable ESD after ferroic engineering and optimizing ~~antiferroelectric~~ field-driven NC, the overall stored energy is still small from an application perspective. Increasing total stored energy requires increasing film thickness while still maintaining the ~~antiferroelectric~~ field-driven NC behavior that underlies the high-ESD performance. This is a challenge for fluorite-structure (anti)ferroelectrics, since its critical thickness is typically limited to the 10-nm regime before the bulk nonpolar monoclinic phase (m-phase, $P2_1/c$) becomes favored[19] (Supplementary Text). Furthermore, scaling up the antiferroelectric thickness is more difficult than the ferroelectric thickness: the t-phase is stable for ultrasmall grain sizes in HZO[27] before it transforms to the o-phase (and subsequently the m-phase) with increasing grain size, which scales with film thickness[27]. ALD nanolaminates i.e. superlattices, can overcome this obstacle, as ferroelectricity and antiferroelectricity persist to the 50-nm regime in ALD-grown fluorite-structure oxides nanolaminated with Al_2O_3[52] and TiO_2[53], respectively.

Learning from these nanolaminate approaches, here we synthesized Al_2O_3-HZO superlattices to scale the desired t-phase symmetry for energy storage applications. For the ALD superlattices, the Al_2O_3 layer was limited to 5 Å thickness, and the HZO layer contains 80% Zr-content based on the baseline 9-nm studies (Fig. 1). Compared to the continuous HZO approach, the superlattice approach aims to maintain the ideal energy storage properties upon increasing thickness, namely (i) ~~antiferroelectric~~ field-induced NC charge boost and (ii) enhanced permittivity during the antiferroelectric to ferroelectric phase transition, and (iii) high breakdown field (Fig.

181 2j). The Al_2O_3 layer thickness should be thick enough to reset the HZO grain growth to main-
182 tain the desired antiferroelectric t-phase while not being too thick to limit the volume fraction of
183 lower-permittivity Al_2O_3 layers. To provide an atomic-scale picture, high-resolution transmission
184 electron microscopy (HR-TEM) compares a continuous ultrathick HZO film (HZOx10 continuous,
185 Fig. 2a, Supplementary Fig. 2) versus the Al_2O_3-HZO superlattice (HZOx10 superlattice, Fig. 2b,
186 Supplementary Fig. 3), both scaled to the 100 nm regime. Cross-sectional TEM for the superlat-
187 tice highlights well-separated Al_2O_3 and HZO layers despite the ultrathin Al_2O_3 interlayers (Fig.
188 2b), consistent with X-ray reflectivity analysis indicating 5 Å Al_2O_3 serves as a sufficient barrier
189 layer, demonstrating clear superlattice reflections (Extended Data Fig. 3). The wavy morphology
190 in the superlattice likely derives from the polycrystalline nature of the HZO layers; the domains
191 in various orientations result in a topology that varies over wide distances, although the films are
192 atomically-smooth over small distances (Extended Data Fig. 3). Therefore, as the ALD Al_2O_3
193 layers conformally coat the HZO surfaces, the rumpled morphology becomes more pronounced
194 with increasing superlattice layers. Despite this topology, the conformal nature of ALD enables
195 the t-phase to persist across the entire thickness, as identified from oxygen imaging analysis of
196 individual HZO superlattice layers (Fig. 2b, Extended Data Fig. 4) and selected area electron
197 diffraction (SAED) indexing analysis of the entire superlattice (Extended Data Fig. 4), while also
198 underscoring the important role of amorphous templating in HZO antiferroelectric-ferroelectric
199 phase stability[54,55]. Furthermore, the superlattice shows similar $d_{101,T}$ lattice spacing as prior work
200 of $\sim$ 9 nm ZrO_2 (Extended Data Fig. 4), demonstrating that the superlattice approach maintains a
201 similar strain state across the entire thickness.

202 The continuous $\sim$ 100 nm HZO film is indexed to the ferroelectric o-phase from both local
203 HR-TEM imaging (Fig. 2b, Extended Data Fig. 5) and electron diffraction (Extended Data Fig. 5),
204 consistent with electrical behavior (Fig. 2c,d). Additionally, the continuous $\sim$ 100 nm HZO film
205 demonstrates similar $d_{111,O}$ lattice spacing as bulk o-phase ZrO_2 (Extended Data Fig. 5), suggest-
206 ing the presence of minimal strain contributions from small size effects.In particular, *C*-*V* loops
207 indicate a thickness-dependent phase evolution from antiferroelectric (10-20 nm) to mixed-ferroic
208 (30-40 nm) to ferroelectric (50-100 nm) behavior (Fig. 2d, Extended Data Fig. 6), in agreement

with the decrease in small-signal permittivity (Fig. 2d, Supplementary Table 2) from $\sim$ 45 (antiferroelectric t-phase) to $\sim$ 30 (ferroelectric o-phase) with increasing thickness. This antiferroelectric-to-ferroelectric transition is consistent with the expected t- to o-phase evolution in HZO, although the o-phase regime extends to higher thicknesses than typically observed (Supplementary Text). In contrast, the *C-V* loops indicate the antiferroelectric electrical behavior persists in the amorphous Al_2O_3-templated HZO superlattices across the thickness space to the 100 nm regime (Fig. 2e), consistent with the structural t-phase indexing (Fig. 2b). Additionally, the small-signal permittivity of the HZO layers, with the Al_2O_3 contribution de-embedded (Methods), is consistent with the antiferroelectric t-phase ($\sim$ 41-48, Fig. 2e, Supplementary Table 2). Furthermore, hysteretic *Q-V* measurements show clear signs of NC (negative *dQ/dV*) for the HZOx10 superlattice (Fig. 2f). Meanwhile the HZOx10 continuous film does not show such NC features (Fig. 2c) – positive *dQ/dV* throughout its entire field space – due to its ferroelectric o-phase structure and thereby no field-driven antiferroelectric-to-ferroelectric phase transition.

To summarize conventional thickness scaling (continuous HZO) versus superlattice thickness scaling (Al_2O_3-HZO) approaches (Fig. 2g,i), the areal ESD is plotted as a function of dielectric thickness (Fig. 2h, Extended Data Fig. 7) and compared against BEOL-compatible capacitors (Supplementary Table 1). The baseline 9-nm antiferroelectric HZO stands above all other BEOL capacitors due to its NC-enhanced energy storage, and the Al_2O_3-templated HZO superlattices approximately linearly scale the areal ESD to the 100 nm regime due to the sustained ~~antiferroelectric~~ field-driven NC behavior (Fig. 2h). Meanwhile, the continuous HZO films begin to saturate with increasing thickness due to the antiferroelectric-to-ferroelectric crossover and corresponding loss of NC and the super-linear Regime II (Fig. 2d, g, Extended Data Fig. 6). The superior energy storage performance of the superlattices is not only due to its maintained ~~antiferroelectric~~ field-driven NC behavior to the ultra-thick regime, but also due to its maintained high breakdown strength relative to the continuous HZO layers (Extended Data Fig. 8d, Supplementary Text), consistent with the significantly lower leakage current present in the superlattices (Extended Data Fig. 8a) and a lower dissipation factor (Supplementary Fig. 4). The conduction mechanism at high fields for both superlattice and continuous HZO films is ascribed to a combination of in-

terface-based Schottky emission and bulk-based Poole-Frenkel emission (Supplementary Fig. 5, Methods). The improved breakdown in the superlattices can be attributed to the Al_2O_3 interlayers better suppressing these emissions, resulting in 2 orders of magnitude lower leakage current (Extended Data Fig. 8a).

Overall, these results indicate oxide superlattices not only offer a practical route towards achieving large ferroic thicknesses for scaling areal ESD (Fig. 2h), but also present a model system to stabilize NC, as demonstrated in ferroelectric-dielectric perovskite[11–13] and fluorite[14] superlattices. In those cases, the additional dielectric layers help depolarize the ferroelectric layer to stabilize steady-state NC. Meanwhile, in this antiferroelectric case, the extra dielectric component from Al_2O_3 does not aid in NC stabilization in the HZO layer at steady-state (Regime I), but rather can contribute to NC stabilization at intermediate electric fields (Regime II) during capacitor charging/discharging (Fig. 2g, Supplementary Fig. 1). Therefore, these demonstrations of NC charge enhancement, including this work, establishes oxide superlattices as a promising materials platform for energy storage. ~~particularly~~ In particular, engineered antiferroelectric superlattices[56,57], as well as classic morphotropic phase boundary systems[58], ~~which demonstrate~~ demonstrating field-driven ferroic phase transitions between antiferroelectric and ferroelectric phases offer new systems to explore for NC realization and can broaden the NC materials space beyond conventional ferroelectrics.

3D-integrated energy storage capacitors The superlattice thickness approach successfully scales the areal ESD (Fig. 2h), and next, to further boost the areal ESD without further increasing thickness, we can implement geometric scaling strategies. In particular, nanostructured storage devices with 3D metal-insulator-metal (MIM) architectures – which require conformal metal and insulator deposition inside porous nanostructures – have successfully increased capacitance density, and therefore energy stored, per unit planar area (Fig. 3b, Supplementary Table 3). Here, we integrated the HZOx10 superlattice into 3D Si trench capacitors with roughly a 100:1 aspect ratio (Methods), facilitated by the conformal nature of ALD. Indeed, TEM imaging and elemental analysis confirms the coverage of the films and the maintenance of the superlattice structure along the trench side-walls down to the trench bottom (Fig. 3a).

Due to the increased volume of material per unit area in 3D trench capacitors (Fig. 3c), the areal capacitance is greatly amplified compared to the 2D planar capacitor case (Fig. 3d). Importantly, the *C-V* results indicate the antiferroelectric behavior is maintained for the Al_2O_3-HZO superlattice in the trench, which is not a trivial assumption due to potential ferroic phase variations introduced by 3D deposition[59,60] (Supplementary Text). Along with the antiferroelectric behavior, the NC behavior also translates to the 3D capacitors (Fig. 3e). The presence of negative *dQ-dV* i.e. NC, is present from the hysteretic *Q-V* loop, and accordingly, the super-linear Regime II derived from this NC behavior is present from the extracted reversible *Q-V* plot (Fig. 3e). Due to the persistence of these key traits, the 3D trench capacitors demonstrate over a 100x boost in areal ESD at 4 MV/cm, with the trench capacitors displaying a recoverable areal ESD of 80 mJ/cm^2 (Fig. 3f). The maximum recoverable areal ESD in the trench has potential to be even higher if it were not for the smeared onset for the super-linear Regime II (Fig. 3e) in conjunction with the reduced breakdown field in the trench (Extended Data Fig. 8). Despite the degraded breakdown strength, reliability is not degraded from an endurance perspective, as the energy density for the HZOx10 superlattice in both planar and trench capacitors survive ~~to 10^9 unipolar cycles (Extended Data Fig. 8)~~ beyond 10^8 unipolar cycles after the onset of Regime II and beyond 10^6 cycles at even higher field cycling (Extended Data Fig. 8), which exceeds that of electrochemical microsupercapacitors and microbatteries (Supplementary Table 4). Moreover, these ultrahigh-ESD trench capacitors take just $\sim$ 250 ns to discharge, leading to 300 kW/cm^2 PD (Fig. 3f, Extended Data Fig. 9).

The NC superlattice integrated into 3D trench capacitors establish record-high ESD (80 mJ/cm^2) and PD (300 kW/cm^2) for electrostatic capacitors by 9x and 170x, respectively (Fig. 3b). The benchmark scatter plot (Fig. 3b) considers areal ESD for the best-performing dielectric electrostatic microcapacitors in 3D-integrated structures, including anodized aluminum oxide, self-rolled structures, nanowires, and Si trenches (Supplementary Table 3). Some of the Si trench results have already integrated antiferroelectric ZrO_2-based dielectrics[59–61], but conventional fluorite-structure antiferroelectric thickness limitations restricted the films to at most 20 nm[60]. Also included are state-of-the-art electrochemical results, including microsupercapacitors

and commercial Li-ion microbatteries (Supplementary Table 4). Due to the inherently slower mechanism of electrochemical energy storage compared to electrostatic, the electrostatic benchmarks display much higher PD (Fig. 3b). And due to the higher capacity mechanism of electrochemical charge storage, electrochemical results display much higher ESD than all of the previous electrostatic benchmarks (Fig. 3b). To overcome this trade-off, through the three-pronged approach of NC ferroic phase engineering, superlattice thickness scaling, and 3D Si trench integration (Extended Data Fig. 1), the 3D NC antiferroelectric capacitors in this work exceed that of many state-of-the-art electrochemical microsupercapacitors (Fig. 3b). Furthermore, the ESD is only $\sim$ 1 order of magnitude away from commercial Li-ion microbatteries ($\sim$ 1 J/cm^2) despite boasting over 8 orders of magnitude larger power density. Therefore, this work overcomes the traditional capacity-speed (ESD-PD) trade-off in energy storage systems (Fig. 3b), which establishes a new paradigm for ultrafast-operation and ultrahigh-density energy storage.

Discussion From a materials perspective, the versatile HfO_2-ZrO_2 system[19,31–34] is atomically-engineered to demonstrate enhanced charge storage via NC superlattices; this establishes a new framework for solid-state supercapacitor materials design which overcomes the conventional permittivity-breakdown trade-off in dielectrics that has previously limited electrostatic energy storage[21] (Extended Data Fig. 10, Supplementary Text). Additionally, the ability to synthesize engineered NC superlattices[11–15] conformally into 3D structure by ALD (Fig. 3a), a well-established large area deposition technique[30], provides unprecedented energy and power density that substantially advances the state-of-the-art in electrostatic capacitors (Fig. 3b) and overcomes the conventional capacity-speed trade-off across the electrostatic-to-electrochemical energy storage hierarchy (Fig. 3b). Furthermore, going beyond traditional energy storage applications, this work accelerates the realization of monolithically-integrated[20] on-chip microcapacitors[2,5,62] for energy storage and power delivery in emerging electronic applications, e.g. Internet of Things devices, advanced edge computing units, and autonomous artificial intelligence agents[3,4,63,64].

1. X. Hao. A review on the dielectric materials for high energy-storage application. *Journal of Advanced Dielectrics*, **03**(01),1330001, (2013).
2. N. A. Kyeremateng, T. Brousse, and D. Pech. Microsupercapacitors as miniaturized energy-storage components for on-chip electronics. *Nature Nanotechnology*, **12**(1),7–15, (2017).
3. C. Lethien, J. Le Bideau, and T. Brousse. Challenges and prospects of 3D micro-supercapacitors for powering the internet of things. *Energy & Environmental Science*, **12**(1),96–115, (2019).
4. P. Simon and Y. Gogotsi. Perspectives for electrochemical capacitors and related devices. *Nature Materials*, **19**(11),1151–1163, (2020).
5. M. Zhu and O. G. Schmidt. Tiny robots and sensors need tiny batteries — here's how to do it. *Nature*, **589**(7841),195–197, (2021).
6. C. A. Aubin, B. Gorissen, E. Milana, P. R. Buskohl, N. Lazarus, G. A. Slipher, C. Keplinger, J. Bongard, F. Iida, J. A. Lewis, and R. F. Shepherd. Towards enduring autonomous robots via embodied energy. *Nature*, **602**(7897),393–402, (2022).
7. M. Salanne, B. Rotenberg, K. Naoi, K. Kaneko, P.-L. Taberna, C. P. Grey, B. Dunn, and P. Simon. Efficient storage mechanisms for building better supercapacitors. *Nature Energy*, **1**(6),16070, (2016).
8. Y. Gogotsi and P. Simon. True Performance Metrics in Electrochemical Energy Storage. *Science*, **334**(6058),917–918, (2011).
9. S. Salahuddin and S. Datta. Use of Negative Capacitance to Provide Voltage Amplification for Low Power Nanoscale Devices. *Nano Letters*, **8**(2),405–410, (2008).
10. A. I. Khan, D. Bhowmik, P. Yu, S. Joo Kim, X. Pan, R. Ramesh, and S. Salahuddin. Experimental evidence of ferroelectric negative capacitance in nanoscale heterostructures. *Applied Physics Letters*, **99**(11),113501, (2011).

343 11. P. Zubko, J. C. Wojdeł, M. Hadjimichael, S. Fernandez-Pena, A. Sené, I. Luk'yanchuk, J.-
344 M. Triscone, and J. Íñiguez. Negative capacitance in multidomain ferroelectric superlattices.
345 *Nature*, **534**(7608),524–528, (2016).

346 12. A. K. Yadav, K. X. Nguyen, Z. Hong, P. García-Fernández, P. Aguado-Puente, C. T. Nelson,
347 S. Das, B. Prasad, D. Kwon, S. Cheema, A. I. Khan, C. Hu, J. Íñiguez, J. Junquera, L.-Q.
348 Chen, D. A. Muller, R. Ramesh, and S. Salahuddin. Spatially resolved steady-state negative
349 capacitance. *Nature*, **565**(7740),468–471, (2019).

350 13. S. Das, Z. Hong, V. A. Stoica, M. A. P. Gonçalves, Y. T. Shao, E. Parsonnet, E. J. Marksz,
351 S. Saremi, M. R. McCarter, A. Reynoso, C. J. Long, A. M. Hagerstrom, D. Meyers, V. Ravi,
352 B. Prasad, H. Zhou, Z. Zhang, H. Wen, F. Gómez-Ortiz, P. García-Fernández, J. Bokor,
353 J. Íñiguez, J. W. Freeland, N. D. Orloff, J. Junquera, L. Q. Chen, S. Salahuddin, D. A. Muller,
354 L. W. Martin, and R. Ramesh. Local negative permittivity and topological phase transition in
355 polar skyrmions. *Nature Materials*, **20**(2),194–201, (2021).

356 14. S. S. Cheema, N. Shanker, L.-C. Wang, C.-H. Hsu, S.-L. Hsu, Y.-H. Liao, M. S. Jose,
357 J. Gomez, W. Chakraborty, W. Li, J.-h. Bae, S. K. Volkman, D. Kwon, Y. Rho, G. Pinelli,
358 R. Rastogi, D. Pipitone, C. Stull, M. Cook, B. Tyrrell, V. A. Stoica, Z. Zhang, J. W. Free-
359 land, C. J. Tassone, A. Mehta, G. Saheli, D. Thompson, D. I. Suh, W.-T. Koo, K.-J. Nam,
360 D. J. Jung, W.-B. Song, C.-H. Lin, S. Nam, J. Heo, N. Parihar, C. P. Grigoropoulos, P. Shafer,
361 P. Fay, R. Ramesh, S. Mahapatra, J. Ciston, S. Datta, M. Mohamed, C. Hu, and S. Salahud-
362 din. Ultrathin ferroic HfO_2-ZrO_2 superlattice gate stack for advanced transistors. *Nature*,
363 **604**(7904),65–71, (2022).

364 15. J. Íñiguez, P. Zubko, I. Luk'yanchuk, and A. Cano. Ferroelectric negative capacitance. *Nature*
365 *Reviews Materials*, **4**(4),243–256, (2019).

366 16. F. Ali, D. Zhou, N. Sun, H. W. Ali, A. Abbas, F. Iqbal, F. Dong, and K.-H. Kim. Fluorite-
367 Structured Ferroelectric-/Antiferroelectric-Based Electrostatic Nanocapacitors for Energy
368 Storage Applications. *ACS Appl. Energy Mater.*, **3**(7),6036–6055, (2020).

369 17. R. Ramesh and D. G. Schlom. Creating emergent phenomena in oxide superlattices. *Nature*
370 *Reviews Materials*, **4**(4),257–268, (2019).

371 18. B. Noheda and G. Catalan. Symmetry engineering and size effects in ferroelectric thin films. In
372 *Handbook of Advanced Dielectric, Piezoelectric and Ferroelectric Materials*, pages 756–795.
373 CRC Press, (2008).

374 19. U. Schroeder, M. H. Park, T. Mikolajick, and C. S. Hwang. The fundamentals and applications
375 of ferroelectric HfO_2. *Nature Reviews Materials*, **7**(8),653–669, (2022).

376 20. M. D. Bishop, H.-S. P. Wong, S. Mitra, and M. M. Shulaker. Monolithic 3-D Integration. *IEEE*
377 *Micro*, **39**(6),16–27, (2019).

378 21. L. Yang, X. Kong, F. Li, H. Hao, Z. Cheng, H. Liu, J.-F. Li, and S. Zhang. Perovskite lead-
379 free dielectrics for energy storage applications. *Progress in Materials Science*, **102**(December
380 2018),72–108, (2019).

381 22. H. Pan, F. Li, Y. Liu, Q. Zhang, M. Wang, S. Lan, Y. Zheng, J. Ma, L. Gu, Y. Shen, P. Yu,
382 S. Zhang, L.-Q. Chen, Y.-H. Lin, and C.-W. Nan. Ultrahigh–energy density lead-free dielectric
383 films via polymorphic nanodomain design. *Science*, **365**(6453),578–582, (2019).

384 23. J. Kim, S. Saremi, M. Acharya, G. Velarde, E. Parsonnet, P. Donahue, A. Qualls, D. Garcia,
385 and L. W. Martin. Ultrahigh capacitive energy density in ion-bombarded relaxor ferroelectric
386 films. *Science*, **369**(6499),81–84, (2020).

387 24. H. Pan, S. Lan, S. Xu, Q. Zhang, H. Yao, Y. Liu, F. Meng, E.-j. Guo, L. Gu, D. Yi, X. Renshaw
388 Wang, H. Huang, J. L. MacManus-Driscoll, L.-q. Chen, K.-j. Jin, C.-w. Nan, and Y.-h. Lin.
389 Ultrahigh energy storage in superparaelectric relaxor ferroelectrics. *Science*, **374**(6563),100–
390 104, (2021).

391 25. H. Qiao, C. Wang, W. S. Choi, M. H. Park, and Y. Kim. Ultra-thin ferroelectrics. *Materials*
392 *Science and Engineering: R: Reports*145100622, (2021).

393 26. D. G. Schlom and J. H. Haeni. A Thermodynamic Approach to Selecting Alternative Gate
394 Dielectrics. *MRS Bull.*, **27**(3),198–204, (2002).

395 27. M. Lederer, D. Lehninger, T. Ali, and T. Kämpfe. Review on the microstructure of ferroelectric
396 hafnium oxides. *physica status solidi (RRL) – Rapid Research Letters*, page 2200168, (2022).

397 28. S. S. Cheema, D. Kwon, N. Shanker, R. dos Reis, S.-L. Hsu, J. Xiao, H. Zhang, R. Wagner,
398 A. Datar, M. R. McCarter, C. R. Serrao, A. K. Yadav, G. Karbasian, C.-H. Hsu, A. J. Tan, L.-C.
399 Wang, V. Thakare, X. Zhang, A. Mehta, E. Karapetrova, R. V. Chopdekar, P. Shafer, E. Aren-
400 holz, C. Hu, R. Proksch, R. Ramesh, J. Ciston, and S. Salahuddin. Enhanced ferroelectricity
401 in ultrathin films grown directly on silicon. *Nature*, **580**(7804),478–482, (2020).

402 29. S. S. Cheema, N. Shanker, S.-L. Hsu, Y. Rho, C.-H. Hsu, V. Stoica, Z. Zhang, J. Freeland,
403 P. Shafer, Grigoropoulos, J. Ciston, and S. Salahuddin. Emergent ferroelectricity in sub-
404 nanometer binary oxide films on silicon. *Science*, **376**(6593),648–652, (2022).

405 30. H. A. Hsain, Y. Lee, M. Materano, T. Mittmann, A. Payne, T. Mikolajick, U. Schroeder, G. N.
406 Parsons, and J. L. Jones. Many routes to ferroelectric HfO_2: A review of current deposition
407 methods. *Journal of Vacuum Science & Technology A*, **40**(1),010803, (2022).

408 31. D. G. Schlom, S. Guha, and S. Datta. Gate Oxides Beyond SiO_2. *MRS Bull.*, **33**(11),1017–
409 1025, (2008).

410 32. T. Mikolajick, S. Slesazeck, M. Park, and U. Schroeder. Ferroelectric hafnium oxide for
411 ferroelectric random-access memories and ferroelectric field-effect transistors. *MRS Bull.*,
412 **43**(5),340–346, (2018).

413 33. S. Salahuddin, K. Ni, and S. Datta. The era of hyper-scaling in electronics. *Nat. Electron.*,
414 **1**(8),442–450, (2018).

415 34. A. I. Khan, A. Keshavarzi, and S. Datta. The future of ferroelectric field-effect transistor
416 technology. *Nature Electronics*, **3**(10),588–597, (2020).

417 35. Y. Wei, P. Nukala, M. Salverda, S. Matzen, H. J. Zhao, J. Momand, A. S. Everhardt, G. Ag-
418 nus, G. R. Blake, P. Lecoeur, B. J. Kooi, J. Íñiguez, B. Dkhil, and B. Noheda. A rhombo-
419 hedral ferroelectric phase in epitaxially strained $Hf_{0.5}Zr_{0.5}O_2$ thin films. *Nature Materials*,
420 **17**(12),1095–1100, (2018).

421 36. H.-J. Lee, M. Lee, K. Lee, J. Jo, H. Yang, Y. Kim, S. C. Chae, U. Waghmare, and J. H. Lee.
422 Scale-free ferroelectricity induced by flat phonon bands in HfO_2. *Science*, **369**(6509),1343–
423 1347, (2020).

424 37. B. Noheda and J. Iniguez. A key piece of the ferroelectric hafnia puzzle. *Science*,
425 **369**(6509),1300–1301, (2020).

426 38. K. Ni, A. Saha, W. Chakraborty, H. Ye, B. Grisafe, J. Smith, G. B. Rayner, S. Gupta, and
427 S. Datta. Equivalent Oxide Thickness (EOT) Scaling With Hafnium Zirconium Oxide High-κ
428 Dielectric Near Morphotropic Phase Boundary. In *2019 IEEE International Electron Devices*
429 *Meeting (IEDM)*, pages 7.4.1–7.4.4. IEEE, (2019).

430 39. P. Nukala, M. Ahmadi, Y. Wei, S. de Graaf, S. Matzen, H. W. Zandbergen, B. Kooi, and
431 B. Noheda. Reversible oxygen migration and phase transitions in hafnia-based ferroelectric
432 devices. *Science*, **372**(6542),630–635, (2021).

433 40. S. Lombardo, C. Nelson, K. Chae, S. Reyes-Lillo, M. Tian, N. Tasneem, Z. Wang, M. Hoff-
434 mann, D. Triyoso, S. Consiglio, K. Tapily, R. Clark, G. Leusink, K. Cho, A. Kummel,
435 J. Kacher, and A. I. Khan. Atomic-scale imaging of polarization switching in an (anti-
436)ferroelectric memory material: Zirconia (ZrO_2). In *2020 IEEE Symposium on VLSI Tech-*
437 *nology*, pages 1–2. IEEE, (2020).

438 41. P. Nukala, Y. Wei, V. de Haas, Q. Guo, J. Antoja-Lleonart, and B. Noheda. Guidelines for the
439 stabilization of a polar rhombohedral phase in epitaxial $Hf_{0.5}Zr_{0.5}O_2$ thin films. *Ferroelectrics*,
440 **569**(1),148–163, (2020).

441 42. M. H. Park, H. J. Kim, Y. J. Kim, T. Moon, K. D. Kim, and C. S. Hwang. Thin $Hf_xZr_{1-x}O_2$

442 Films: A New Lead-Free System for Electrostatic Supercapacitors with Large Energy Storage
443 Density and Robust Thermal Stability. *Advanced Energy Materials*, **4**(16),1400610, (2014).

444 43. M. H. Park and C. S. Hwang. Fluorite-structure antiferroelectrics. *Reports on Progress in*
445 *Physics*, **82**(12),124502, (2019).

446 44. F. Ali, T. Ali, D. Lehninger, A. Sünbül, A. Viegas, R. Sachdeva, A. Abbas, M. Czernohorsky,
447 K. Seidel, and T. Kämpf. Fluorite-Structured Ferroelectric and Antiferroelectric Materials: A
448 Gateway of Miniaturized Electronic Devices. *Adv. Funct. Mater.*, **32**(27),2201737, (2022).

449 45. Z. Wang, A. A. Gaskell, M. Dopita, D. Kriegner, N. Tasneem, J. Mack, N. Mukher-
450 jee, Z. Karim, and A. I. Khan. Antiferroelectricity in lanthanum doped zirconia without
451 metallic capping layers and post-deposition/-metallization anneals. *Applied Physics Letters*,
452 **112**(22),222902, (2018).

453 46. N. Tasneem, Y. M. Yousry, M. Tian, M. Dopita, S. E. Reyes-Lillo, J. Kacher, N. Bassiri-
454 Gharb, and A. I. Khan. A Janovec-Kay-Dunn-Like Behavior at Thickness Scaling in Ultra-
455 Thin Antiferroelectric ZrO_2 Films. *Adv. Electron. Mater.*, **7**(11),2100485, (2021).

456 47. A. I. Khan, K. Chatterjee, B. Wang, S. Drapcho, L. You, C. Serrao, S. R. Bakaul, R. Ramesh,
457 and S. Salahuddin. Negative capacitance in a ferroelectric capacitor. *Nature Materials*,
458 **14**(2),182–186, (2015).

459 48. M. Hoffmann, F. P. G. Fengler, B. Max, U. Schroeder, S. Slesazeck, and T. Mikola-
460 jick. Negative Capacitance for Electrostatic Supercapacitors. *Advanced Energy Materials*,
461 **9**(40),1901154, (2019).

462 49. M. Hoffmann, Z. Wang, N. Tasneem, A. Zubair, P. V. Ravindran, M. Tian, A. A. Gaskell,
463 D. Triyoso, S. Consiglio, K. Tapily, R. Clark, J. Hur, S. S. K. Pentapati, S. K. Lim, M. Dopita,
464 S. Yu, W. Chern, J. Kacher, S. E. Reyes-Lillo, D. Antoniadis, J. Ravichandran, S. Slesazeck,
465 T. Mikolajick, and A. I. Khan. Antiferroelectric negative capacitance from a structural phase
466 transition in zirconia. *Nature Communications*, **13**(1),1228, (2022).

467 50. L. Qiao, C. Song, Y. Sun, M. U. Fayaz, T. Lu, S. Yin, C. Chen, H. Xu, T.-l. Ren, and F. Pan.
468 Observation of negative capacitance in antiferroelectric $PbZrO_3$ Films. *Nature Communica-*
469 *tions*, **12**(1),4215, (2021).

470 51. F. Li, S. Zhang, D. Damjanovic, L.-Q. Chen, and T. R. Shrout. Local Structural Heterogeneity
471 and Electromechanical Responses of Ferroelectrics: Learning from Relaxor Ferroelectrics.
472 *Advanced Functional Materials*, **28**(37),1801504, (2018).

473 52. S. Riedel, P. Polakowski, and J. Müller. A thermally robust and thickness independent ferro-
474 electric phase in laminated hafnium zirconium oxide. *AIP Advances*, **6**(9),095123, (2016).

475 53. S.-H. Yi, H.-C. Lin, and M.-J. Chen. Ultra-high energy storage density and scale-up of an-
476 tiferroelectric $TiO_2/ZrO_2/TiO_2$ stacks for supercapacitors. *Journal of Materials Chemistry A*,
477 **9**(14),9081–9091, (2021).

478 54. S. F. Lombardo, M. Tian, K. Chae, J. Hur, N. Tasneem, S. Yu, K. Cho, A. C. Kummel,
479 J. Kacher, and A. I. Khan. Local epitaxial-like templating effects and grain size distribu-
480 tion in atomic layer deposited $Hf_{0.5}Zr_{0.5}O_2$ thin film ferroelectric capacitors. *Applied Physics*
481 *Letters*, **119**(9),092901, (2021).

482 55. K. Chae, S. F. Lombardo, N. Tasneem, M. Tian, H. Kumarasubramanian, J. Hur, W. Chern,
483 S. Yu, C. Richter, P. D. Lomenzo, M. Hoffmann, U. Schroeder, D. Triyoso, S. Consiglio,
484 K. Tapily, R. Clark, G. Leusink, N. Bassiri-Gharb, P. Bandaru, J. Ravichandran, A. Kummel,
485 K. Cho, J. Kacher, and A. I. Khan. Local Epitaxial Templating Effects in Ferroelectric and
486 Antiferroelectric ZrO_2. *ACS Applied Materials & Interfaces*, **14**(32),36771–36780, (2022).

487 56. J. A. Mundy, B. F. Grosso, C. A. Heikes, D. Ferenc Segedin, Z. Wang, Y.-T. Shao, C. Dai,
488 B. H. Goodge, Q. N. Meier, C. T. Nelson, B. Prasad, F. Xue, S. Ganschow, D. A. Muller,
489 L. F. Kourkoutis, L.-q. Chen, W. D. Ratcliff, N. A. Spaldin, R. Ramesh, and D. G. Schlom.
490 Liberating a hidden antiferroelectric phase with interfacial electrostatic engineering. *Science*
491 *Advances*, **8**(5),9, (2022).

492 57. L. Caretta, Y.-T. Shao, J. Yu, A. B. Mei, B. F. Grosso, C. Dai, P. Behera, D. Lee, M. McCarter,
493 E. Parsonnet, H. K. P, F. Xue, X. Guo, E. S. Barnard, S. Ganschow, Z. Hong, A. Raja, L. W.
494 Martin, L.-Q. Chen, M. Fiebig, K. Lai, N. A. Spaldin, D. A. Muller, D. G. Schlom, and
495 R. Ramesh. Non-volatile electric-field control of inversion symmetry. *Nature Materials*,
496 **22**(2),207–215, (2023).

497 58. B. Noheda and D. E. Cox. Bridging phases at the morphotropic boundaries of lead oxide solid
498 solutions. *Phase Transitions*, **79**(1-2),5–20, (2006).

499 59. K. Kühnel, M. Czernohorsky, C. Mart, and W. Weinreich. High-density energy storage in
500 Si-doped hafnium oxide thin films on area-enhanced substrates. *Journal of Vacuum Science &*
501 *Technology B*, **37**(2),021401, (2019).

502 60. A. Viegas, C. Mart, and M. Czernohorsky. Antiferroelectric Si:HfO_2 for High Energy Storage
503 using 3D MIM Capacitors. In *2020 Joint Conference of the IEEE International Frequency*
504 *Control Symposium and International Symposium on Applications of Ferroelectrics (IFCS-*
505 *ISAF)*, pages 1–3. IEEE, (2020).

506 61. M. Pešić, M. Hoffmann, C. Richter, T. Mikolajick, and U. Schroeder. Nonvolatile Random
507 Access Memory and Energy Storage Based on Antiferroelectric Like Hysteresis in ZrO_2. *Ad-*
508 *vanced Functional Materials*, **26**(41),7486–7494, (2016).

509 62. P. Gargini, F. Balestra, and Y. Hayashi. Roadmapping of Nanoelectronics for the New Elec-
510 tronics Industry. *Applied Sciences*, **12**(1),308, (2021).

511 63. A. Keshavarzi and W. van den Hoek. Edge Intelligence—On the Challenging Road to a Trillion
512 Smart Connected IoT Devices. *IEEE Design & Test*, **36**(2),41–64, (2019).

513 64. A. Keshavarzi, K. Ni, W. Van Den Hoek, S. Datta, and A. Raychowdhury. FerroElectronics
514 for Edge Intelligence. *IEEE Micro*, **40**(6),33–48, (2020).

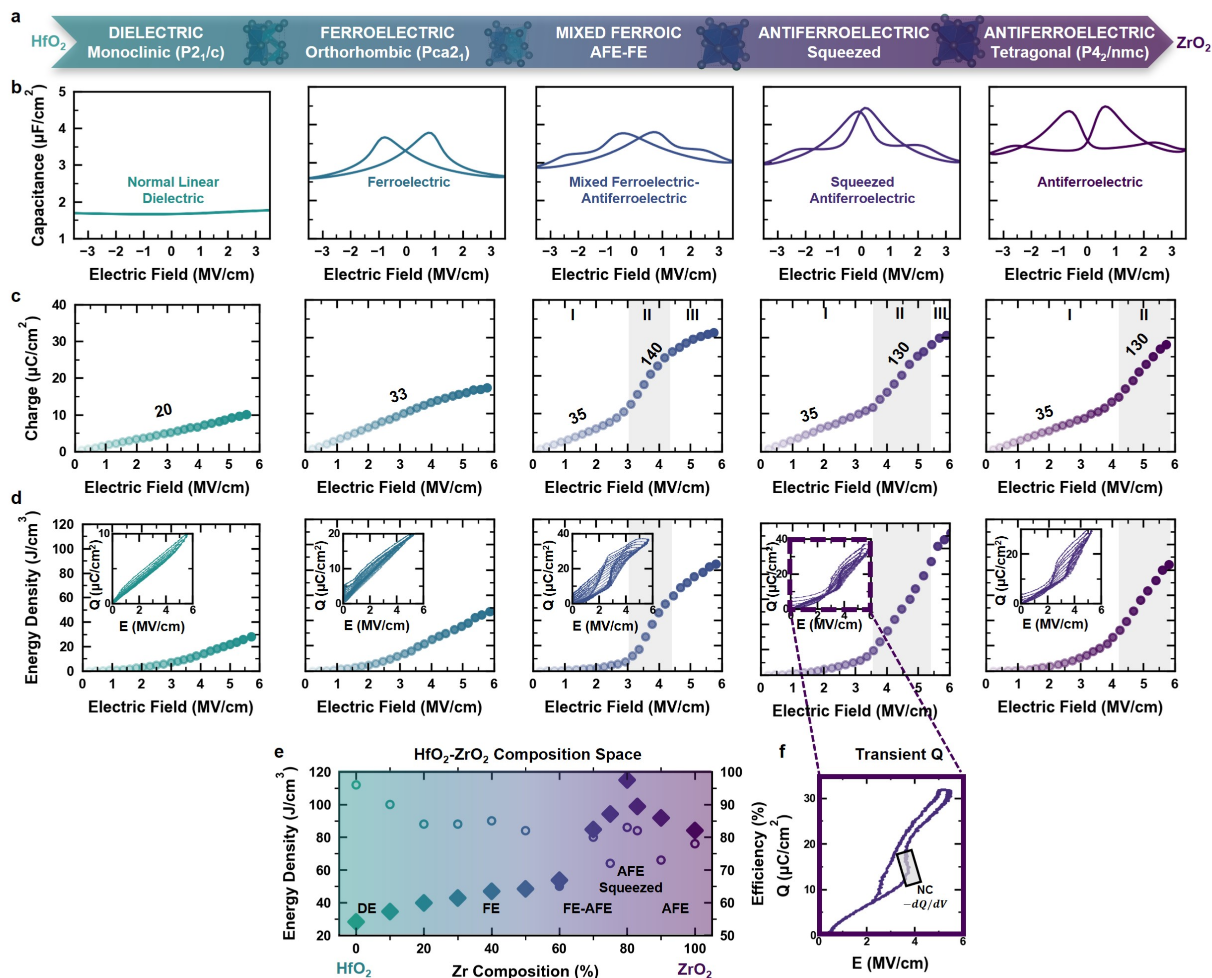

515

516 **Fig. 1. | Ultrahigh energy storage via ferroic phase engineering and negative capacitance**
517 **in HfO_2-ZrO_2.** **(a)** Dielectric-ferroelectric-antiferroelectric (DE-FE-AFE) ferroic phase space
518 in fluorite-structure HfO_2-ZrO_2 binary oxide thin films. **(b, c, d)** Capacitance (b), reversible stored
519 charge (c), and electrostatic energy storage density (ESD, d) as a function of electric field spanning
520 the ferroic phase space (left to right: DE, FE, mixed FE-AFE, squeezed AFE, and AFE). Inset to
521 D: hysteretic charge-field curves used to extract ESD. Capacitance-electric field was measured via
522 small-signal electrical measurements (Methods), while the reversible stored charge-electric field
523 and electrostatic energy storage density-electric field were extracted from pulsed *I-V* measure-
524 ments (Methods, Extended Data Fig. 2). **(e)** Electrostatic ESD and efficiency as a function of Zr
525 composition. The largest ESD is reported for the squeezed AFE HZO (80% Zr), in which the onset

of the phase transition to the FE state is lowered closer to zero field compared to the normal AFE state at 100% Zr composition; this leads to a earlier onset of the enhanced energy storage during Regime II. **(f)** Hysteretic charge-electric field curve for the squeezed AFE shows a negative slope (dQ/dE) – which corresponds to negative capacitance (NC) – in the intermediate field regime (Regime II) corresponding to the AFE t-phase to FE o-phase conversion. ~~**(g)** Energy landscape evolution of AFE HZO as it transforms from native AFE t-phase (left, Regime I, pink) to mixed t-o phase (center, Regime II, black) to fully FE o-phase (right, Regime III, purple) with increasing field. In Regime II, the flattened energy landscape from AFE-FE phase competition enhances permittivity and stabilizes NC in the FE o-phase fraction, leading to the charge-boosted behavior.~~

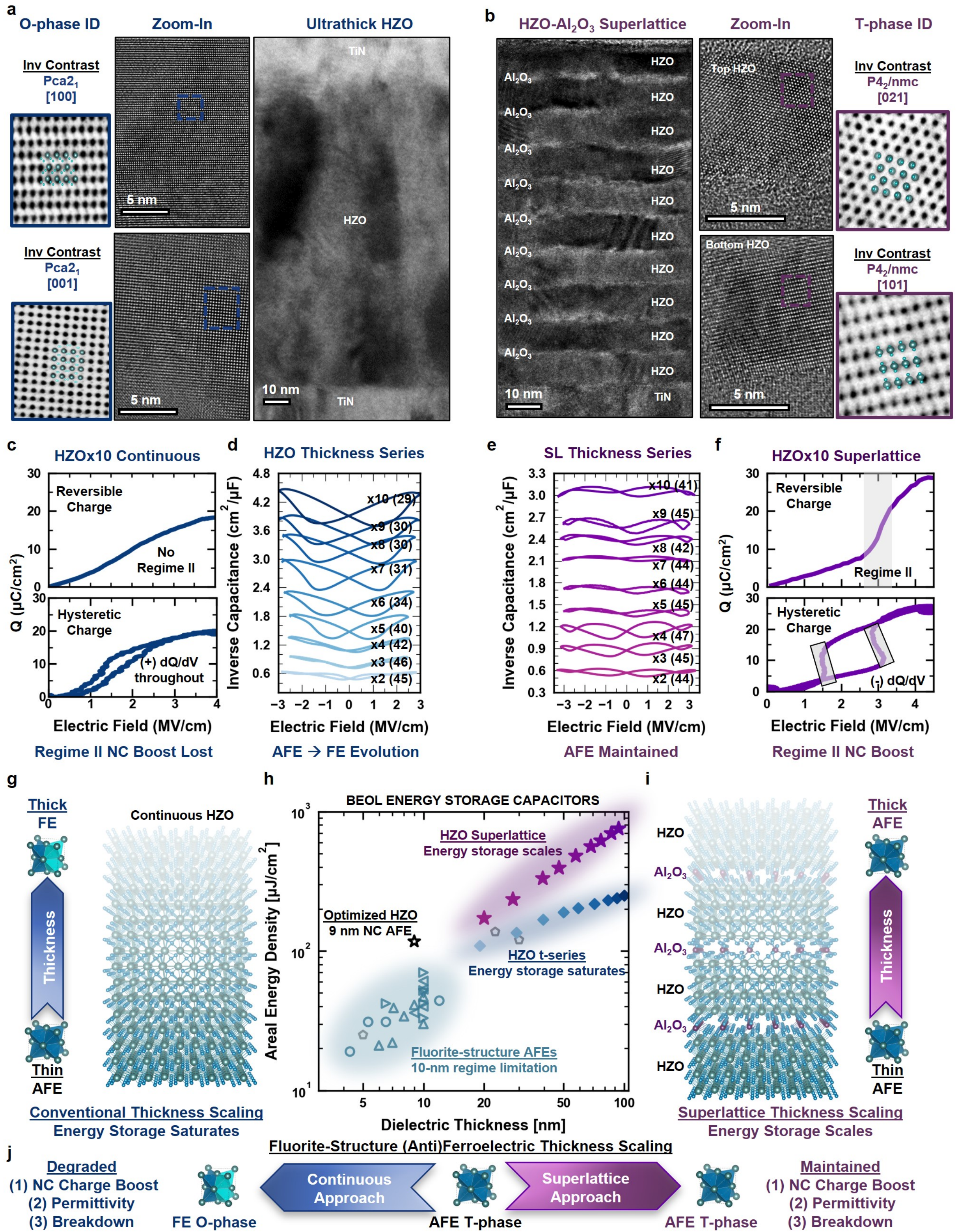

535

Fig. 2. | Scaling up total energy storage via HZO-Al_2O_3 antiferroelectric negative capacitance superlattices. Maintaining the antiferroelectric phase and large breakdown field at large thicknesses enhances the scaling of the total energy stored. **(a, b)** Cross-sectional HR-TEM images of a $\sim$ 100 nm thick HZO film (continuous HZOx10) (a, right) and HZO-Al_2O_3 superlattice film (superlattice HZOx10) (b, left). Zoomed-in regions HR-TEM images (a center, b center) are indexed to the o-phase (a, left) and t-phase (b, right) for the continuous thick HZO and the HZO-Al_2O_3 superlattice, respectively (Extended Data Fig. 4, 5). For inverted contrast images (a left, b right), light (dark) atoms represent O (Hf, Zr) atoms. **(c-f)** Thickness evolution of ferroic and NC behavior via continuous (c, d) and superlattice (e, f) approaches. (c, f) Reversible charge (top) and hysteretic charge (bottom) as a function of field for continuous HZOx10 (c) and superlattice HZOx10 (f). (d, e) Capacitance-electric field (*C*-*E*) behavior as a function of thickness for continuous (d) and superlattice approaches (e). For each thickness, the small-signal permittivity is annotated; for the superlattice approach, the permittivity is reported with the Al_2O_3 contribution de-embeded (Methods, Supplementary Table 2). The superlattice approach maintains antiferroelectric behavior and expected small-signal permittivity ($\sim$ 41-48, Supplementary Table 2) across the entire thickness range (e) while the continuous approach shows an antiferroelectric-ferroelectric phase evolution past 40 nm (d), in agreement with the decrease in small-signal permittivity (Supplementary Table 2) from $\sim$ 45 (antiferroelectric t-phase) to $\sim$ 30 (ferroelectric o-phase). Additionally, the superlattice approach maintains the super-linear Regime II and NC behavior (indicated by the negative slope in the hysteretic *Q*-*E* curve) to the 100 nm regime (f), while the continuous approach does not (c) due to its evolution to the ferroelectric phase. **(g, i)** Schematic of continuous HZO (g) and superlattice HZO-Al_2O_3 superlattice structure (i) and corresponding ferroic phase evolution with increasing thickness. **(h)** Areal ESD as a function of dielectric thickness for the continuous and superlattice HZO thickness series to the 100-nm regime. The results are compared against BEOL-compatible MIM capacitors, namely fluorite-structure HfO_2-ZrO_2-based antiferroelectrics (green) and thicker ALD-grown dielectric oxides (grey) (Supplementary Table 1). **(j)** Fluorite-structure antiferroelectric-ferroelectric phase evolution as a function of increasing thickness via continuous (left) and superlattice (right) approaches.

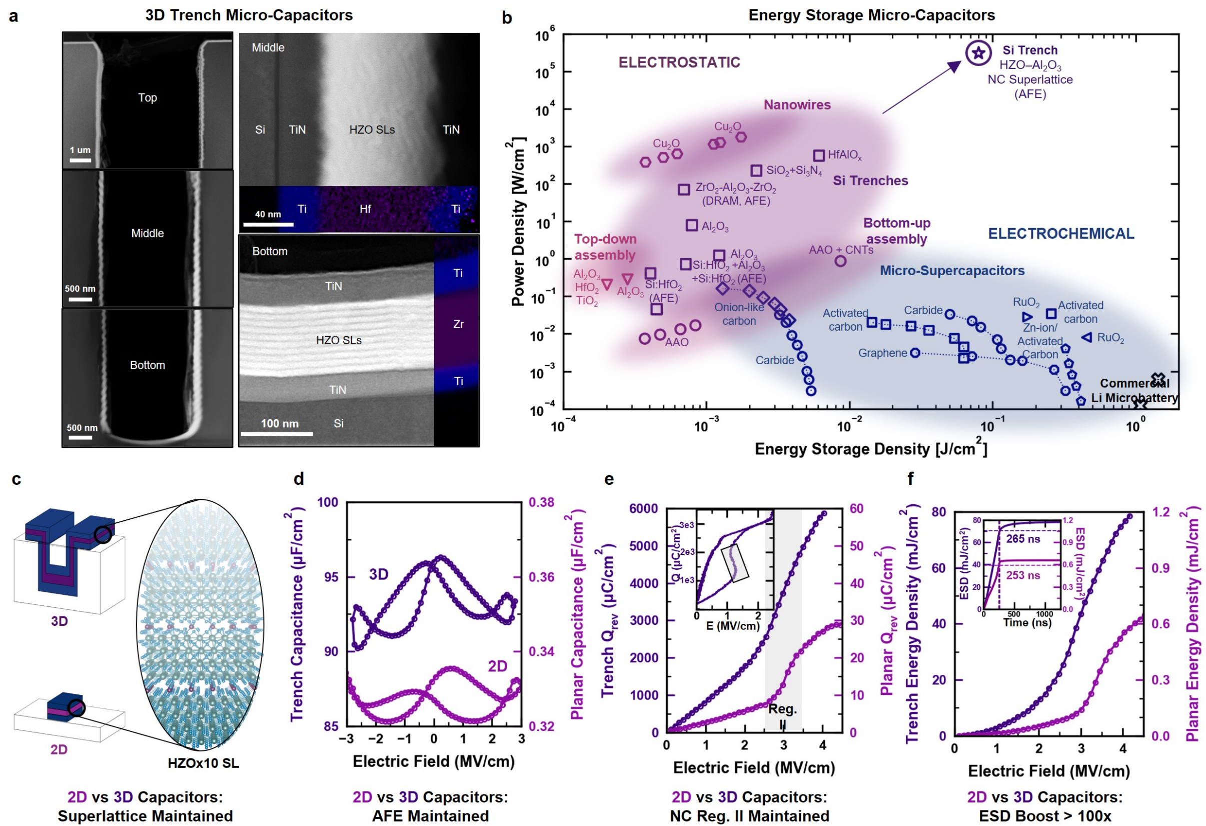

Fig. 3. | **3D-integrated antiferroelectric negative capacitance microcapacitors on Si. (a)** TEM mapping of the ∼ 100-nm HZO-Al_2O_3 superlattice conformally filling a 3D trench capacitor (∼100 μm depth) on Si. Zoomed-in images of the trench sidewalls and trench indicate the HZO-Al_2O_3 superlattice structure is maintained (upper right, lower right), and elemental analysis confirms the expected HZO composition is also maintained in the trench (Supplementary Fig. 8). **(b)** Power density versus energy storage density for the highest-reported microcapacitors. The benchmark includes various 3D-integrated electrostatic structures: nanowires (light purple, hexagons), top-down-assembled self-rolled structures (pink, triangles), bottom-up-assembled anodized aluminum oxide (AAO) structures (purple, circles), and Si trenches (dark purple, squares) (Supplementary Table 3). Si trenches results include fluorite-structure antiferroelectrics integrated into trenches[59,61], denoted by "AFE". State-of-the-art electrochemical microsupercapacitors (blue) and commercial Li-ion microbatteries (black) are also included (Supplementary Table 4). **(c)** Schematic of 3D trench (top) and 2D planar (bottom) capacitors filled with the ∼ 100-nm HZO-

578 Al_2O_3 superlattice (right). **(d)** Capacitance-electric field behavior for planar and trench capacitors,
579 illustrating enhanced capacitance per projected area and the persistence of the antiferroelectric be-
580 havior in the trenches. **(e)** Reversible charge as function of electric field for planar and trench
581 capacitors. Inset: Hysteretic charge as a function of electric field indicating the NC behavior
582 (Regime II) persists in the trench capacitor. **(f)** Recoverable energy storage density as function of
583 electric field for planar and trench capacitors. The trench capacitor shows over 100x ESD enhance-
584 ment compared to planar capacitor due to the ~~antiferroelectric~~ field-driven NC behavior translating
585 from planar to trench structures. Inset: Discharge measurements for planar and trench capacitors
586 demonstrating $\sim$ 250 ns discharge time (Extended Data Fig. 9, Methods), from which the trench
587 capacitor power density is determined in (b).

588 **Methods**

589 **Synthesis and Processing** All thin film synthesis was performed at U.C. Berkeley; device pro-
590 cessing was performed at the U.C. Berkeley Marvell Nanofabrication Laboratory and MIT Lincoln
591 Laboratory.

592 **Dielectric film deposition** Thin films of HfO_2-ZrO_2 (HZO) and Al_2O_3-HZO superlattices
593 were grown by atomic layer deposition (ALD) in a Fiji Ultratech/Cambridge Nanotech tool at
594 270°C. Tetrakis (ethylmethylamido) hafnium (IV) [TEMAH; $Hf(NCH_3C_2H_5)_4$], Tetrakis (ethyl-
595 methylamido) zirconium (IV) [TEMAZ; $Zr(NCH_3C_2H_5)_4$], Trimethylaluminum [TMA; $Al(CH_3)_3$]
596 and water (H_2O) were used as Hf, Zr, Al, and oxygen sources, respectively. The ALD growth tech-
597 nique facilitates atomic-level thickness control required for superlattices and conformal deposition
598 required for 3D trench capacitors[65]. Further ALD details on HZO (anti)ferroelectric phase stabi-
599 lization[28,29] and ALD nanolaminates[66] to scale HZO-based ferroelectricity[67] can be found in the
600 referenced works.

601 **2D planar capacitor fabrication** Si wafers were cleaned in Piranha (120°C for 10 min-
602 utes) to remove organics and HF (50:1 H_2O:HF at room temperature for 30 s) to remove any native
603 oxide. For the bottom metal, $\sim$ 20 nm of TiN was deposited by plasma-enhanced ALD at 400°C
604 with tetrakis (dimethylamido) titanium (IV) [TDMAT; $[(CH_3)_2N]_4Ti$] precursor and N_2 plasma.
605 Subsequently, the HZO or Al_2O_3-HZO superlattices is deposited at 270°C by ALD. For the top
606 metal, $\sim$ 20 nm of TiN was deposited by plasma-enhanced ALD at 400°C followed by $\sim$ 60 nm of
607 sputtered W at room temperature. Finally, the top electrodes are defined by photolithography and
608 selective etching of the top metal electrode.

609 **3D Si trench capacitor fabrication** Si trenches (areal footprint of approximately 50 μm
610 $\times$ 1 μm, Supplementary Fig. 6) are first formed by photolithographic patterning of a Si wafer,
611 followed by etching $\sim$ 100 μm deep with a time-multiplexed deep reactive ion etch process. The
612 etch process consists of rapidly alternating between an isotropic Si etch step and a deposition step
613 for sidewall passivation, repeated until the desired depth is reached. This process enables the for-

614 mation of high aspect ratio features using a simple photoresist mask. Afterward, the trenches are
615 cleaned in Piranha (120°C for 10 minutes) to remove organics and HF (50:1 H_2O:HF at room tem-
616 perature for 30 s) to remove any native oxide. Then, the TiN/Al_2O_3-HZO/TiN MIM is deposited
617 via ALD followed by $\sim$ 60 nm of sputtered W at room temperature. Finally, top electrodes are
618 defined by photolithography and selective etching of the top metal electrodes.

619 **Thin film characterization**

620 **Transmission electron microscopy** High resolution TEM/STEM experiments were per-
621 formed with an aberration-corrected FEI Themis 60-300 TEM/STEM microscope equipped with
622 a Ceta2 camera operated in electron-counting mode operated at 300 kV at the National Center
623 for Electron Microscopy (NCEM) facility of the Molecular Foundry at Lawrence Berkeley Na-
624 tional Laboratory (LBNL). Cross-sectional samples of both planar and 3D Si trench capacitors
625 were fabricated by the FEI Helios G4 UX dual beam Focused Ion Beam (FIB) with final milling
626 at 0.5 keV and mechanical polishing using an Allied High Tech Multiprep at a 0.5° with a Gatan
627 Precision Ion Milling System to an electron-transparent specimen with final milling at 200 eV.
628 For accurate phase identification of the continuous and superlattice HZOx10 samples, oxygen-
629 sensitive negative spherical aberration imaging (NCSI)[68–70] was used to probe both the cation and
630 anion sublattices. In particular, local oxygen atomic imaging is important to distinguish between
631 the nearly identical polar o-phase and nonpolar t-phases[29,39,70,71]. HR-TEM simulations (Supple-
632 mentary Fig. 7) were calculated approximately close to the experimental conditions using the
633 Prismatic method[72–74]. The high-contrast morphology of 3D Si trench capacitors were acquired
634 using a FEI Titan TEM/STEM microscope operated at 300 kV to confirm the conformal deposi-
635 tion, and energy dispersive X-ray spectroscopy (EDS) was used for elemental mapping (Fig. 3a,
636 Supplementary Fig. 8). For the EDS mapping, the microscope is equipped with four windowless
637 silicon drift detectors with a total solid angle of 0.7 steradians and 140 eV energy resolution. The
638 EDS mappings were acquired at 300 kV with a probe current of $\sim$ 400 pA, 40 μm C_2 aperture,
639 0.46 nm step size, and a total acquisition time of approximately 10 minutes with a dwell time of
640 0.83 ms.

NCSI & HR-TEM simulations As a function of defocus (C_1) and specimen thickness, the simulations of ferroelectric $Pca2_1$ and antiferroelectric $P4_2/nmc$ phases were calculated under the following experimental conditions: C_s = -16 μm, C_5 = 6.8 mm, slice thickness = 2 nm, and accelerating voltage = 300 kV. The $P4_2/nmc$ simulations indicate that the oxygen atoms become visible at appropriate defocus values ($\sim$ 2 to 4 nm) and reasonable specimen thicknesses (below 12.25 nm), which is similar to the experimental oxygen imaging conditions as expected to be visible for specimen thicknesses around 10 nm[75] (Supplementary Fig. 7). Therefore, the HR-TEM simulations for the tetragonal $P4_2/nmc$ [021] (specimen thickness = 10.8 nm, defocus = 4 nm), [001] (specimen thickness = 9.8 nm, defocus = 4 nm), and [101] (specimen thickness = 12.7 nm, defocus = 2 nm) zone axes were found to match well with the Al_2O_3-HZO superlattices experimental data (Extended Data Fig. 4-5, Supplementary Fig. 7). As for the orthorhombic $Pca2_1$ phase, the HR-TEM simulations of [100] (specimen thickness = 31.81 nm, Defocus: 8 nm) and [001] (specimen thickness = 36.45 nm, Defocus: 8 nm) were found to match closely with the cation sublattices of thick HZO cation sublattice (Extended Data Fig. 5, Supplementary Fig. 9), ruling out the presence of monoclinic $P2_1/c$ phase. Further information about NCSI analysis for fluorite-structure ferroic phase identification is provided in our previous work[29].

Selected area electron diffraction Selected area electron diffraction (SAED) was performed on a FEI ThemIS microscope operating voltage at 300 kV, and the data was acquired with an integration time of 500 ms at a camera length of 770 mm on a Ceta2 4k x 4k camera to form final 2k x 2k images. The SAED patterns of HZOx10 continuous and HZOx10 superlattice structures exhibit bright single crystal spot patterns coming from silicon substrate and polycrystalline concentric diffuse ring patterns originating from HfO_2-ZrO_2 and TiN. Indexing the radial profile integration spectra, the HZOx10 superlattice film indexes to the t-phase (Extended Data Fig. 4) and the HZOx10 continuous film indexes primarily to the o-phase (Extended Data Fig. 5). The HZOx10 continuous film also shows the presence of some m-phase (Extended Data Fig. 5), which is consistent with the expected phase evolution with increasing thickness in which larger grain sizes favor m-phase stabilization[19].

668 **X-ray reflectivity** X-ray reflectivity (XRR) was measured with the Panalytical X'Pert Pro
669 system, and thickness fitting was performed with Panalytical software (Extended Data Fig. 3)
670 to determine the thickness of $\sim$ 9 nm HZO films of varying composition (Fig. 1), ultrathick
671 continuous HZO films (Fig. 2), and HZO-Al_2O_3 superlattice films (Fig. 2, Extended Data Fig. 3).
672 The growth rate – 0.9-1.0 Å/cycle – is consistent with ALD-grown HfO_2-ZrO_2 as demonstrated in
673 our previous work[14,28,29].

674 **Atomic force microscopy** The roughness of the 9 nm HZO (80% Zr), HZOx10 super-
675 lattice, and HZOx10 continuous films (Extended Data Fig. 3) were extracted from atomic force
676 microscopy (AFM) measurements using a commercial scanning probe microscope (MFP-3D, Asy-
677 lum Research). All topography measurements were carried out using silicon AFM probe tips
678 (Tap300Al-G BudgetSensor) with a force constant of 40 (Nm^{-1}) at a resonance frequency of $\sim$300
679 kHz using the AC Air Topography mode (non-contact tapping mode).

680 **Dielectric and electrical measurements**

681 **Metal-insulator-metal (MIM) capacitance and leakage current** Capacitance-voltage (*C*-
682 *V*) measurements (Fig. 1b, Fig. 2e,f, Fig. 3d, Extended Data Fig. 6) were performed using a
683 commercial Semiconductor Device Analyzer (Agilent B1500) with a multi-frequency capacitance
684 measuring unit at frequencies ranging from 1-100 kHz. Electrical contact was made using 19 μm
685 (DCP-HTR 154-001, FormFactor) tips within a commercial probe station (Cascade Microtech);
686 voltage was applied to the top electrode and the bottom electrode was grounded.

687 **MIM impedance measurements** Frequency-dependent impedance measurements (Ex-
688 tended Data Fig. 2, Supplementary Fig. 4) were performed using a HP4194A Impedance/Gain-
689 Phase Analyzer. A short-open calibration was performed before impedance measurements. Impedance
690 (amplitude-phase) measurements were then carried out ranging from 1-1000 kHz with voltage ap-
691 plied to the top electrode and the bottom electrode was grounded.

692 **Permittivity extraction of Al_2O_3 from Al_2O_3 thickness series** The permittivity of Al_2O_3
693 was extracted from thickness-dependent (4.5 nm, 6 nm, 8 nm) Al_2O_3 MIM with TiN electrodes
694 measurements (Supplementary Fig. 10). Since inverse capacitance is a linear function of the film
695 thickness, the permittivity can be extracted from the slope. A permittivity of 9 (Supplementary Fig.
696 10) was extracted for Al_2O_3, consistent with the Al_2O_3 permittivity extracted in prior works[14].

Permittivity extraction of HZO layers in HZO-Al_2O_3 superlattices For the HZOxN superlattice samples, the permittivity of just the HZO layers can be calculated by de-embedding out the contribution of the Al_2O_3 layers via the relation:

$$\frac{1}{C_{\text{HZO}}} = \frac{1}{C_{\text{total}}} - \frac{1}{C_{\text{Al}_2\text{O}_3}}$$

697 Each Al_2O_3 layer was assumed to have 5 Å thickness and a permittivity of 9 (Supplementary
698 Fig. 10).

699 **Polarization-voltage measurements** Polarization-voltage (P-V) measurements (Supple-
700 mentary Fig. 11) were performed using a Radiant ferroelectric tester. The Radiant ferroelectric
701 tester allowed for the application of higher voltages needed to measure thicker films. A triangular
702 waveform was applied at 10 kHz to obtain the extracted P-V loops.

703 **Series resistance extraction from impedance measurements** To reliably extract the ESD
704 from fast pulsed I-V measurements, the parasitic series resistance (R_s) must be reliably extracted
705 so that the voltage across across the capacitor can be reliably determined. The series resistance is
706 the sum of parasitic resistances of the setup and the resistance of the sample electrodes. Without
707 accounting for R_s, larger hysteresis will be observed, which will lead to underestimated ESD
708 values. Series resistance considerations are not critical in conventional P-V measurements as the
709 capacitor charging current ($I_c = C\frac{dV}{dt}$) is not large enough to have a considerable voltage drop
710 across the series resistance as $\frac{dV}{dt}$ is not large and therefore the voltage drop across the capacitor
711 can be assumed to be equal to the applied voltage pulse. To extract R_s, frequency-dependent
712 impedance measurements were performed. ~~using a HP4194A Impedance/Gain-Phase Analyzer.~~

713 ~~A short-open calibration was performed before impedance measurements. Impedance (amplitude-~~
714 ~~phase) measurements were then carried out ranging from 1-1000 kHz with voltage applied to the~~
715 ~~top electrode and the bottom electrode was grounded.~~ A three-component circuit (Extended Data
716 Fig. 2k) consisting of R_s in series to a parallel combination of a capacitor, C, and R_p (which models
717 the leakage flow across the capacitor) was used to fit the measured impedance versus frequency
718 data. The complex impedance of the three-component circuit is given by,

$$Z = R_s + \frac{R_p}{1 + j\omega R_p C}, \tag{1}$$

where ω is the angular frequency. Taking the real and imaginary parts, we have

$$Re(Z) = R_s + \frac{R_p}{1 + \omega^2 R_p^2 C^2} \tag{2}$$

$$Im(Z) = \frac{-\omega R_p C}{1 + \omega^2 R_p^2 C^2}. \tag{3}$$

719 Therefore, the series resistance can be extracted by,

$$R_s = \lim_{\omega \to \infty} Re(Z). \tag{4}$$

720 An example R_s extraction for 9 nm HZO (80% Zr) is show in Extended Data Fig. 2g-j. The real
721 (Extended Data Fig. 2i) and imaginary (Extended Data Fig. 2j) parts of the complex impedance fit
722 well to the 3 component circuit model. From the real part at high frequencies, R_s was extracted to
723 be 155Ω and is bias independent, as expected.

724 **Pulsed *I-V* measurements** Pulsed current–voltage (*I-V*) measurements were performed
725 on both 2D and 3D MIM capacitor structures to extract the charge-electric field (*Q-E*) and *ESD-E*
726 characteristics, following similar measurements detailed in our previous work[28]. Electrical contact
727 was made using 19 μm (DCP-HTR 154-001, FormFactor) tips within a commercial probe sta-
728 tion (Cascade Microtech); voltage was applied to the top electrode, and the bottom electrode was
729 grounded. For voltage pulses below 40 V, the capacitor structures were connected to a LabView-
730 controlled B1525A high voltage semiconductor pulse generator unit (HV-SPGU) and the current
731 and voltage was measured through an InfiniiVision DSOX3024A oscilloscope with 50 Ω and 1

732 MΩ input impedances, respectively. In particular, the voltage was measured with N2843A passive
733 probes with a 500 MHz bandwidth, 10:1 attenuation ratio, and input resistance of 10 MΩ, while
734 the current was calculated from the voltage drop across the 50 Ω input impedance by terminating
735 the circuit with a co-axial BNC cable to the oscilloscope's 50 Ω input impedance. For voltage
736 pulses above 40 V, the voltage pulses were generated via a half bridge inverter circuit, where two
737 complementary switches (EPC2218 GaN transistors) convert a DC voltage generated from an Ag-
738 ilent E3649A power supply into a pulsed voltage waveform. The pulsed waveform is generated
739 by first turning on (off) switch 1 (2) during the rise time, where switch 1 is connected to the DC
740 supply's positive output and switch 2 is connected to a common ground. Subsequently, switch 2
741 (1) is turned on (off) to ramp the output voltage down to ground during the fall time of the pulse.
742 A microcontroller (Arduino Leonardo) was programmed to provide the clock signals to turn the
743 switches on/off.

744 Furthermore, since energy storage devices are unipolar devices, for practical application we
745 must look at the non-switching *I-V* transients, as there will be no voltage of the opposite polarity to
746 switch any ferroelectric polarization that may be present. Thus, first a "pre-poling" pulse (Extended
747 Data Fig. 2c inset) corresponding to the maximum voltage is applied to the capacitor to remove any
748 ferroelectric switching contributions to the subsequent voltage pulses. Then voltage pulses (500-
749 2000 ns with 50-200 ns rise/fall times) with increasing amplitudes were applied to the capacitor
750 and the current was measured. This measurement scheme has been previously used to characterize
751 antiferroelectric HZO capacitors for DRAM applications[76].

752 **Pulsed charge-voltage extraction** From the pulsed *I-V* measurements, the current is in-
753 tegrated to obtain the charge vs time (*Q-t*) curve and is normalized by the areal footprint of the
754 device. From the charge transients, three parameters are extracted for each voltage pulse: the max-
755 imum charge stored in the capacitor during charging, Q_{max}; the residual charge on the capacitor
756 after the capacitor is discharged, Q_{res}; and their difference, $Q_{rev} = Q_{max} - Q_{res}$. Of these three
757 parameters, Q_{rev} is the most important from an application standpoint as it is the charge can be
758 reversibly stored and released[28,77]. Q_{res} can be interpreted as the charge that was stored through
759 leakage current of the capacitor.

760 To construct the pulsed *Q*-*E* curves, the electric field was calculated as $E = \frac{\max(V - I_{leak}(R_s + R_{osc}))}{t_{HZO}}$,
761 where I_{leak} is the leakage current which can be found as the current after the capacitive charg-
762 ing current transient, R_s is the extracted series resistance, and R_{osc} is the oscilloscope's input
763 impedance, which was set to 50 Ω. $I_{leak}(R_{osc} + R_s)$ can be interpreted as the voltage drop across
764 the series parasitic and oscilloscope resistances due to the leakage current flowing through the
765 capacitor. The charge is equal to Q_{rev}.

766 **ESD extraction from pulsed *I*-*V* measurements** The ESD extraction methodology is
767 summarized in Extended Data Fig. 2. From the pulsed *I*-*V* measurements, the current is inte-
768 grated to obtain the charge vs time (*Q*-*t*) curve and is normalized by the areal footprint of the
769 device. Without any R_s correction, when *Q*-*V* is plotted directly (Extended Data Fig. 2l), a large
770 hysteresis is observed that is inflated due to R_s.

771 To construct the hysteretic *Q*-*E* curves, the electric field is calculated as $E = \frac{V - I(R_{osc} + R_s)}{t_{HZO}}$,
772 where R_s is the series resistance and R_{osc} is the oscilloscope input resistance (50 Ω) and the charge
773 is Q. From the series resistance corrected *Q*-*E* curves, the energy storage density for each voltage
774 is calculated as,

$$ESD = -\int_{Q_{max}}^{Q_r} EdQ \text{ (discharging branch)} \tag{5}$$

775 where Q_{max} is the maximum charge and Q_r is the remnant charge on the capacitor. The efficiency,
776 η, is calculated as:

$$\eta = \frac{-\int_{Q_{max}}^{Q_r} EdQ \text{ (discharging branch)}}{\int_0^{Q_{max}} EdQ \text{ (charging branch)}} \tag{6}$$

ESD from conventional *P*-*V* measurements From the *P*-*V* measurements, the energy storage density and efficiency (η) were extracted by:

$$ESD = -\int_{P_{max}}^{P_r} EdP \text{ (discharging branch)} \tag{7}$$

$$\eta = \frac{-\int_{P_{max}}^{P_r} EdP \text{ (discharging branch)}}{\int_0^{P_{max}} EdP \text{ (charging branch)}} \tag{8}$$

777 **Comparison of ESD extraction procedures** The main difference between the ESD ex-
778 traction from conventional *P*-*V* measurements and pulsed *I*-*V* measurements is the measurement

779 speed. The *P*-*V* measurements were measured at low frequencies ($\sim$1-10 kHz), where the dis-
780 charging process is on the order of 100 μs, in contrast to the pulsed *I*-*V* measurements where the
781 capacitors are discharged in 50-200 ns, three orders of magnitude faster. Due to this difference
782 in time scales, ESD extraction from conventional *P*-*V* loops tend to show larger ESD compared
783 to faster ESD measurement protocols[21]. In this work, a similar difference was observed; the con-
784 ventional *P*-*V* measurements show larger ESD at slightly lower fields compared to the pulsed *I*-*V*
785 measurements, although the overall ESD calculated from both methods are similar (Supplementary
786 Fig. 11). Additionally, the faster measurement speeds of the pulsed *I*-*V* measurements allows for
787 evaluation of the maximum power density of these energy storage capacitors. For all of the figures
788 and benchmarks, the ESD extracted from pulsed *I*-*V* measurements are considered.

789 **Power Density Extraction** The power densities for the HZOx10 superlattice integrated
790 in both planar (Extended Data Fig. 9a-d) and trench (Extended Data Fig. 9e-h) was extracted
791 from the discharging branch of the voltage pulse. From the discharge current (Extended Data Fig.
792 9b,f), the power dissipated (Extended Data Fig. 9c, g) was calculated by $P = IV$, where I is the
793 discharge current and V is the R_s-corrected voltage across the capacitor. To extract the average
794 power density, the discharge time was calculated by the amount of time it took to release 90% of
795 the stored energy[21] (Extended Data Fig. 9d,h) and the average power density was calculated by
796 $P = ESD/t_{discharge}$.

797 **Reliability characterization** Leakage current-voltage (*I*-*V*) measurements (Extended Data
798 Fig. 8a) were performed using a commercial Semiconductor Device Analyzer (Agilent B1500).
799 Endurance was characterized by applying unipolar pulses (1 μs pulsewidth and 100 ns rise/fall
800 times) with an B1525A HV-SPGU at ~~2.5 MV/cm~~ two electric fields (1 μs pulses) – one near the
801 onset of Regime II (3.0 MV/cm and 2.5 MV/cm for planar and trench, respectively) and another at
802 0.5 MV/cm higher field – and measuring the ESD with pulsed *I*-*V* measurements (Extended Data
803 Fig. 8b, c). Breakdown strength (Extended Data Fig. 8e, f) was evaluated by testing 15 devices

804 until failure and fitting their distribution to a two-parameter Weibull distribution[21], given by:

$$P(E_i) = 1 - \exp\left(-\left(\frac{E_i}{E_b}\right)^{\beta}\right) \tag{9}$$

805 where E_i is the breakdown field of device i, $P(E_i)$ is the cumulative probability, E_b is the char-
806 acteristic breakdown strength corresponding to a cumulative probability of 63.2% of the tested
807 devices, and β is the Weibull parameter which describes the variation of breakdown field.

808 **Leakage current modelling** The leakage current of HZOx10 continuous and superlattice
809 films were fit to different conduction mechanisms commonly found in oxide dielectric thin films
810 (Supplementary Fig. 5)[78]. These include bulk-limited mechanisms, such as Ohmic conduction,
811 space-charge limited conduction (SCLC), and Poole-Frenkel (P-F) emission, and interface-limited
812 mechanisms, such as Fowler-Nordheim (F-N) tunneling and Schottky emission.

For the above conduction mechanisms, the current density (J) and electric field (E) are proportional to each other via the following relationships[78,79]:

$$\text{Ohmic: } \log_{10}(J) \propto \log_{10}(E)$$

$$\text{SCLC: } \log_{10}(J) \propto 2\log_{10}(E)$$

$$\text{P-F emission: } \ln\left(\frac{J}{E}\right) \propto \frac{1}{k_B T}\left(\frac{q^3}{\pi\epsilon_0 K}\right) E^{1/2}$$

$$\text{Schottky emission: } \ln(J) \propto \frac{1}{k_B T}\left(\frac{q^3}{4\pi\epsilon_0 K}\right) E^{1/2}$$

$$\text{F-N tunneling: } \ln\left(\frac{J}{E^2}\right) \propto \frac{1}{E}$$

813 where q, k_B, T, ϵ_0 and K are the electronic charge, Boltzmann constant, temperature, vacuum per-
814 mittivity, and optical permittivity, respectively. Note that the optical permittivity (K) is given by
815 n^2, where n is the index of refraction. For HfO_2-ZrO_2, the index of refraction is $\sim$ 1.95-2.15[80].

Methods References

65. R. W. Johnson, A. Hultqvist, and S. F. Bent. A brief review of atomic layer deposition: from fundamentals to applications. *Materials Today*17236–246, (2014).

66. J. Y. Park, D. H. Lee, K. Yang, S. H. Kim, G. T. Yu, G. H. Park, E. B. Lee, K. H. Kim, and M. H. Park. Engineering Strategies in Emerging Fluorite-Structured Ferroelectrics. *ACS Applied Electronic Materials*, **4**(4),1369–1380, (2022).

67. H. J. Kim, M. H. Park, Y. J. Kim, Y. H. Lee, W. Jeon, T. Gwon, T. Moon, K. D. Kim, and C. S. Hwang. Grain size engineering for ferroelectric $Hf_{0.5}Zr_{0.5}O_2$ films by an insertion of Al_2O_3 interlayer. *Applied Physics Letters*, **105**(19),192903, (2014).

68. C. L. Jia, M. Lentzen, and K. Urban. Atomic-Resolution Imaging of Oxygen in Perovskite Ceramics. *Science*, **299**(5608),870–873, (2003).

69. C. Jia, L. Houben, A. Thust, and J. Barthel. On the benefit of the negative-spherical-aberration imaging technique for quantitative HRTEM. *Ultramicroscopy*, **110**(5),500–505, (2010).

70. H. Du, C. Groh, C.-L. Jia, T. Ohlerth, R. E. Dunin-Borkowski, U. Simon, and J. Mayer. Multiple polarization orders in individual twinned colloidal nanocrystals of centrosymmetric HfO_2. *Matter*, **4**(3),986–1000, (2021).

71. P. Nukala, M. Ahmadi, J. Antoja-Lleonart, S. de Graaf, Y. Wei, H. W. Zandbergen, B. J. Kooi, and B. Noheda. In situ heating studies on temperature-induced phase transitions in epitaxial $Hf_{0.5}Zr_{0.5}O_2/La_{0.67}Sr_{0.33}MnO_3$ heterostructures. *Applied Physics Letters*, **118**(6),062901, (2021).

72. A. Pryor, C. Ophus, and J. Miao. A streaming multi-GPU implementation of image simulation algorithms for scanning transmission electron microscopy. *Advanced Structural and Chemical Imaging*, **3**(1),15, (2017).

73. C. Ophus. A fast image simulation algorithm for scanning transmission electron microscopy. *Advanced Structural and Chemical Imaging*, **3**(1),13, (2017).

841 74. L. Rangel DaCosta, H. G. Brown, P. M. Pelz, A. Rakowski, N. Barber, P. O'Donovan,
842 P. McBean, L. Jones, J. Ciston, M. Scott, and C. Ophus. Prismatic 2.0 – Simulation software
843 for scanning and high resolution transmission electron microscopy (STEM and HRTEM). *Mi-*
844 *cron*151103141, (2021).

845 75. K. W. Urban, C. L. Jia, L. Houben, M. Lentzen, S. B. Mi, and K. Tillmann. Negative spher-
846 ical aberration ultrahigh-resolution imaging in corrected transmission electron microscopy.
847 *Philosophical Transactions of the Royal Society A: Mathematical, Physical and Engineering*
848 *Sciences*, **367**(1903),3735–3753, (2009).

849 76. S. D. Hyun, H. W. Park, M. H. Park, Y. H. Lee, Y. B. Lee, B. Y. Kim, H. H. Kim, B. S. Kim,
850 and C. S. Hwang. Field-Induced Ferroelectric $Hf_{1-x}Zr_xO_2$ Thin Films for High-κ Dynamic
851 Random Access Memory. *Adv. Electron. Mater.*, **6**(11),2000631, (2020).

852 77. Y. J. Kim, H. Yamada, T. Moon, Y. J. Kwon, C. H. An, H. J. Kim, K. D. Kim, Y. H. Lee,
853 S. D. Hyun, M. H. Park, and C. S. Hwang. Time-Dependent Negative Capacitance Effects in
854 Al_2O_3/$BaTiO_3$ Bilayers. *Nano Letters*, **16**(7),4375–4381, (2016).

855 78. F.-C. Chiu. A Review on Conduction Mechanisms in Dielectric Films. *Advances in Materials*
856 *Science and Engineering*20141–18, (2014).

857 79. H. Pan, Q. Zhang, M. Wang, S. Lan, F. Meng, J. Ma, L. Gu, Y. Shen, P. Yu, Y. Lin, and C. Nan.
858 Enhancements of dielectric and energy storage performances in lead-free films with sandwich
859 architecture. *Journal of the American Ceramic Society*, **102**(3),936–943, (2019).

860 80. J. F. Ihlefeld, T. S. Luk, S. W. Smith, S. S. Fields, S. T. Jaszewski, D. M. Hirt, W. T. Riffe,
861 S. Bender, C. Constantin, M. V. Ayyasamy, P. V. Balachandran, P. Lu, M. David Henry, and
862 P. S. Davids. Compositional dependence of linear and nonlinear optical response in crystalline
863 hafnium zirconium oxide thin films. *Journal of Applied Physics*, **128**(3),034101, (2020).

864 81. K. Ni, J. Smith, H. Ye, B. Grisafe, G. B. Rayner, A. Kummel, and S. Datta. A Novel Ferroelec-
865 tric Superlattice Based Multi-Level Cell Non-Volatile Memory. In *2019 IEEE International*
866 *Electron Devices Meeting (IEDM)*, pages 28.8.1–28.8.4. IEEE, (2019).

867 82. T. Ali, R. Olivo, M. Lederer, R. Hoffmann, P. Steinke, K. Zimmermann, U. Muhle, K. Seidel,
868 J. Muller, P. Polakowski, K. Kuhnel, M. Czernohorsky, T. Kampfe, M. Rudolph, B. Patzold,
869 D. Lehninger, and F. Muller. A Multilevel FeFET Memory Device based on Laminated HSO
870 and HZO Ferroelectric Layers for High-Density Storage. pages 28.7.1–28.7.4. IEEE, (2019).

871 83. K. A. Aabrar, J. Gomez, S. G. Kirtania, M. S. Jose, Y. Luo, P. G. Ravikumar, P. V. Ravindran,
872 H. Ye, S. Banerjee, S. Dutta, A. I. Khan, S. Yu, and S. Datta. BEOL Compatible Superlattice
873 FerroFET-based High Precision Analog Weight Cell with Superior Linearity and Symmetry. In
874 *2021 IEEE International Electron Devices Meeting (IEDM)*, volume 2, pages 19.6.1–19.6.4.
875 IEEE, (2021).

876 84. J. Antoja-Lleonart, S. Zhou, K. de Hond, S. Huang, G. Koster, G. Rijnders, and B. Noheda.
877 Atomic layer deposition of SiO_2–GeO_2 multilayers. *Applied Physics Letters*, **117**(4),041601,
878 (2020).

879 85. J. Müller, T. S. Böscke, U. Schröder, S. Mueller, D. Bräuhaus, U. Böttger, L. Frey, and T. Miko-
880 lajick. Ferroelectricity in Simple Binary ZrO_2 and HfO_2. *Nano Letters*, **12**(8),4318–4323,
881 (2012).

882 86. E. H. Kisi, C. J. Howard, and R. J. Hill. Crystal Structure of Orthorhombic Zirconia in Partially
883 Stabilized Zirconia. *Journal of the American Ceramic Society*, **72**(9),1757–1760, (1989).

Acknowledgements This research was supported in part by the following: ASCENT, one of the six centres in the JUMP initiative, a SRC program sponsored by DARPA; U.S. Department of Energy, Office of Science, Office of Basic Energy Sciences, Materials Sciences and Engineering Division under contract no. DE-AC02-05-CH11231 (Codesign of Ultra-Low-Voltage Beyond CMOS Microelectronics) for the development of materials for low-power microelectronics; the Berkeley Center for Negative Capacitance Transistors (BCNCT). Work at the Molecular Foundry was supported by the Office of Science, Office of Basic Energy Sciences, of the U.S. Department of Energy under Contract No. DE-AC02-05CH11231. This material is based upon work supported by the Secretary of Defense for Research and Engineering under Air Force contract no. FA8702-15-D-0001. Any opinions, findings, conclusions or recommendations expressed in this material are those of the author(s) and do not necessarily reflect the views of the Secretary of Defense for Research and Engineering. S.S.C. and N.S. would like to thank to R. Ramesh for characterization facilities and M. Hoffman for LabView setup help.

Author contributions S.S.C. conceived the idea and designed the experiments. S.S.C. and N.S. performed film synthesis and ferroic phase optimization. N.S. performed dielectric and electrical measurements. J.S, N.M.E, and N.S. developed the high voltage pulse generator setup. S.S.C. performed X-ray characterization. S.-L.H. performed transmission electron microscopy. M.M., R.R. and M.C. designed the 3D capacitor structures. N.S., R.R., and M.C. performed capacitor fabrication. 2D and 3D capacitor structures were fabricated at the UC Berkeley Marvell Nanofabrication Laboratory and the MIT Lincoln Laboratory Microelectronics Laboratory, respectively. S.S.C and N.S analyzed all results. S.S.C. and N.S. wrote the manuscript with contributions from S.S. S.S. supervised the research. All authors contributed to discussions and manuscript preparations.

Supplementary information Supplementary Information is available for this paper.

Competing interests The authors declare that they have no competing financial interests.

Correspondence and requests for materials should be addressed to S.S.C. (s.cheema@berkeley.edu) and S.S. (sayeef@berkeley.edu).

Data availability The authors declare that the data supporting the findings of this study are available within the paper and its supplementary information files.

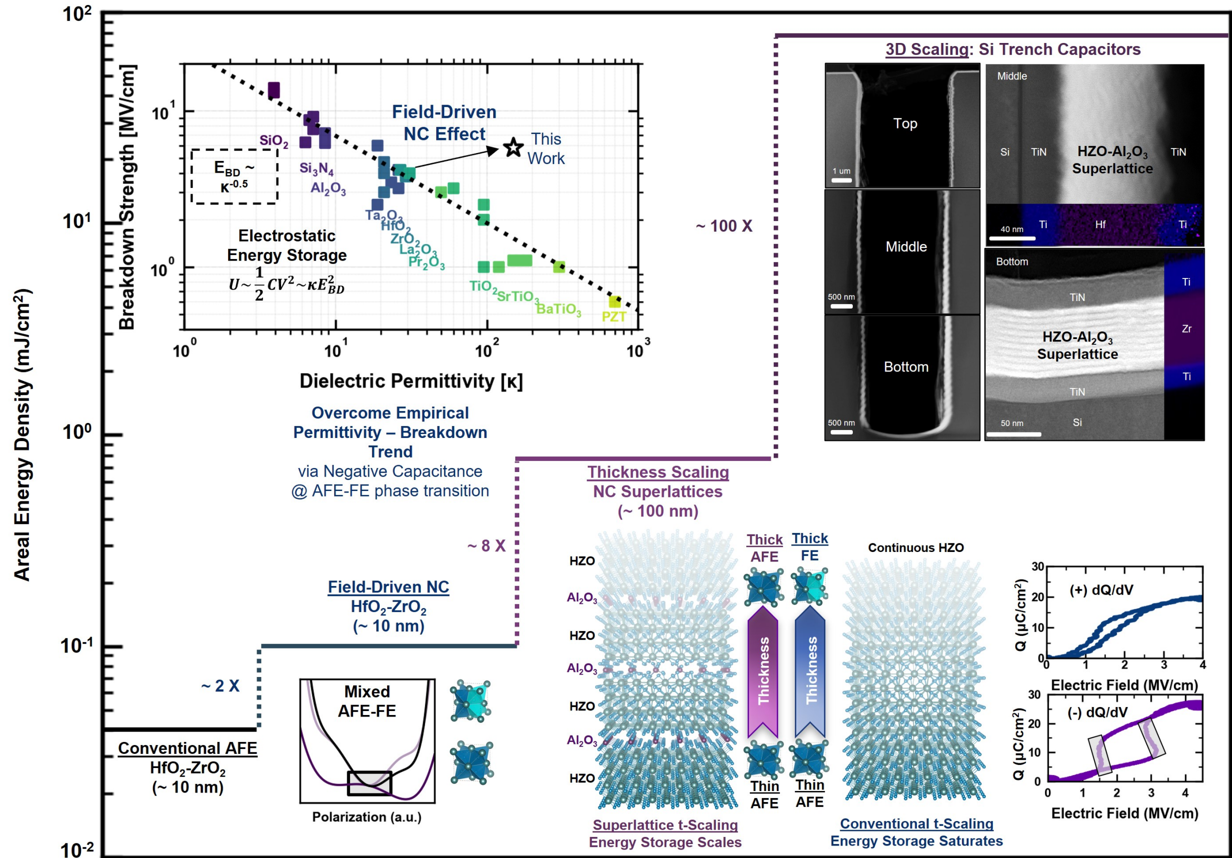

Extended Data Fig. 1. Energy storage engineering strategy. The energy storage density in HZO thin films was optimized through a three-pronged approach: (i) ~~antiferroelectric~~ field-driven NC optimization through ferroic phase engineering in ∼ 10 nm films (left), (ii) scaling up the ~~antiferroelectric~~ field-driven NC behavior to ∼ 100 nm through amorphous-templated superlattices (lower right), and (iii) integration of ~~antiferroelectric~~ NC superlattices into 3D Si capacitors to increase the energy storage density per footprint area (upper right).

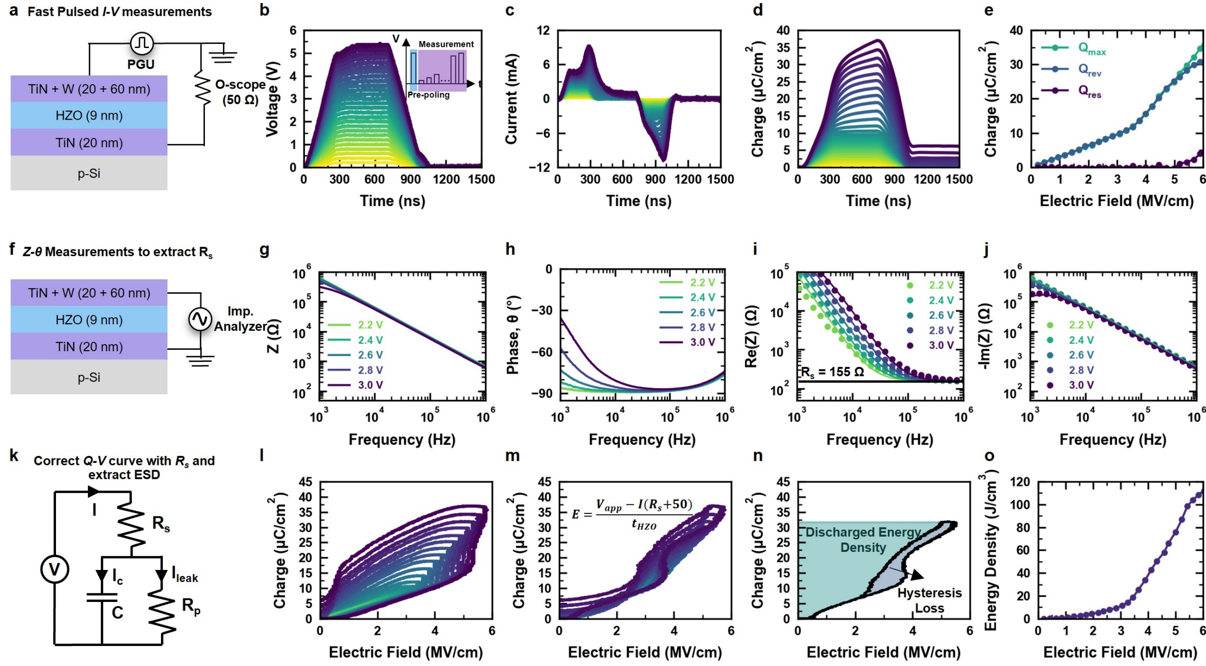

Extended Data Fig. 2. Dielectric energy storage measurement and methodology **(a)** Experimental setup for pulsed *I*-*V* measurements. The pulsed voltage is applied with a pulse generator unit (PGU, Methods), while the current is measured through the oscilloscope's 50 Ω input impedance. **(b, c, d)** The applied voltage pulses (b), measured current response (c), and integrated charge (d) as a function of time for a 9 nm HZO (80% Zr) film. **(e)** The maximum charge Q_{max}, residual charge Q_{res}, and their difference Q_{rev}, derived from the charge versus time curve for each voltage pulse (Methods). Q_{rev} is the charge that is reversibly stored and released from the capacitor. **(f)** Experimental setup for impedance analyzer measurements. **(g, h)** Measured magnitude ($|Z|$, g) and phase (θ, h) of the complex impedance at different biases as a function of frequency. **(i, j)** Fitted real (i) and imaginary (j) parts of the complex impedance assuming a three-component circuit model (k). The series resistance can be found from real part at high frequency (Methods) and should be bias-independent as shown in (i). The series resistance was found to be 155 Ω. **(k)** The three-component circuit model used to correct for the series resistance, where R_s is the series resistance and R_p is the parallel resistance which models the leakage through the capacitor, C. **(l)** The measured hysteretic charge-voltage curve from pulsed *I*-*V* measurements without any series

934 resistance correction. **(m)** The R_s-corrected hysteretic *Q*-*V* curves corresponding to each voltage
935 pulse applied. Note that 50 Ω was added to R_s extracted in (i) due to the additional 50 Ω from
936 the oscilloscope's input impedance. **(n)** The extracted energy storage density (ESD) is taken to be
937 the shaded green area, which can be calculated by $\int_{Q_{rem}}^{Q_{max}} EdQ$ (Methods). The shaded blue area
938 represents the hysteretic energy loss during the charging-discharging cycle. **(o)** The extracted ESD
939 as a function of electric field for 9 nm HZO (80% Zr).

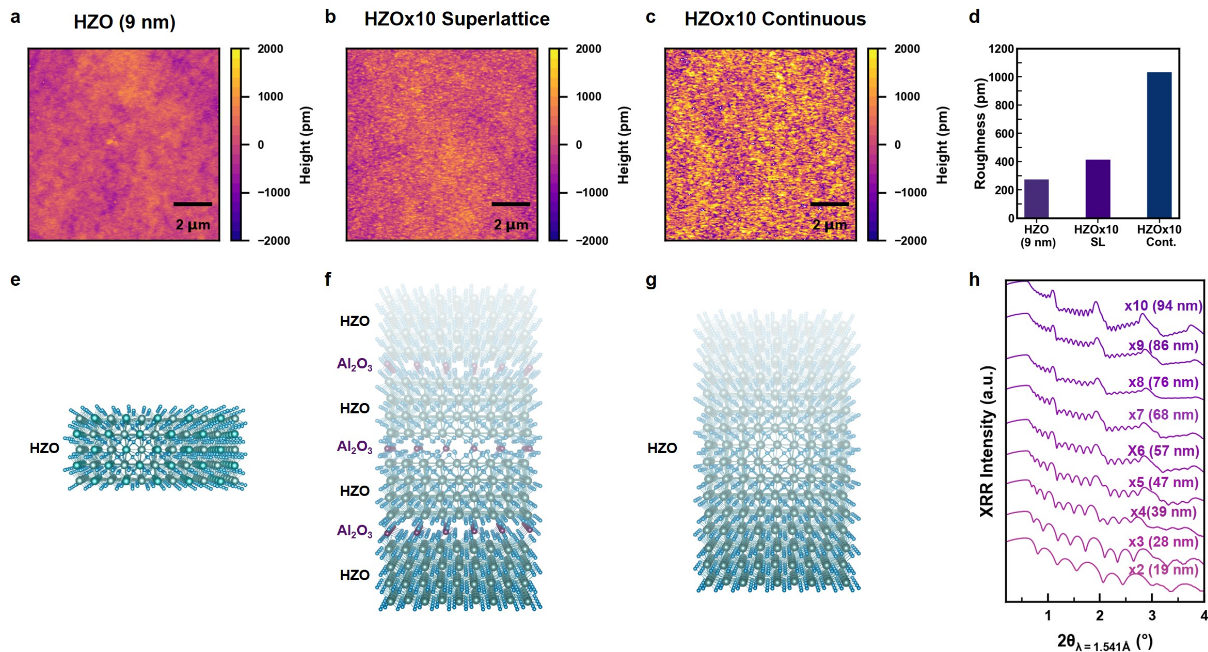

940

941 **Extended Data Fig. 3. Superlattice Structure and Morphology Characterization (a, b, c)**
942 AFM topography for the 9 nm HZO film (80% Zr, a), HZOx10 superlattice (b), and HZOx10 con-
943 tinuous (c) films. **(d)** Extracted rms roughness values for each film, demonstrating the persistence
944 of smooth films for the HZO-Al_2O_3 superlattice. **(e, f, g)** Schematic of 9 nm HZO (e), HZOx10
945 superlattice (f), and HZOx10 continuous (g) films. **(h)** X-ray reflectivity (XRR) of HZOx2-10
946 superlattice films. Clear superlattice reflections are observed, which indicate that the thin (0.5
947 nm) Al_2O_3 layers serve as a sufficient barrier to separate the HZO layers, consistent with TEM
948 (Extended Data Fig. 4) and recent HfO_2-based superlattice engineering studies[52, 67,81–83]. In fact,
949 ALD of binary oxide superlattices have demonstrated the absence of chemical intermixing down
950 to atomic layer periodicity[84].

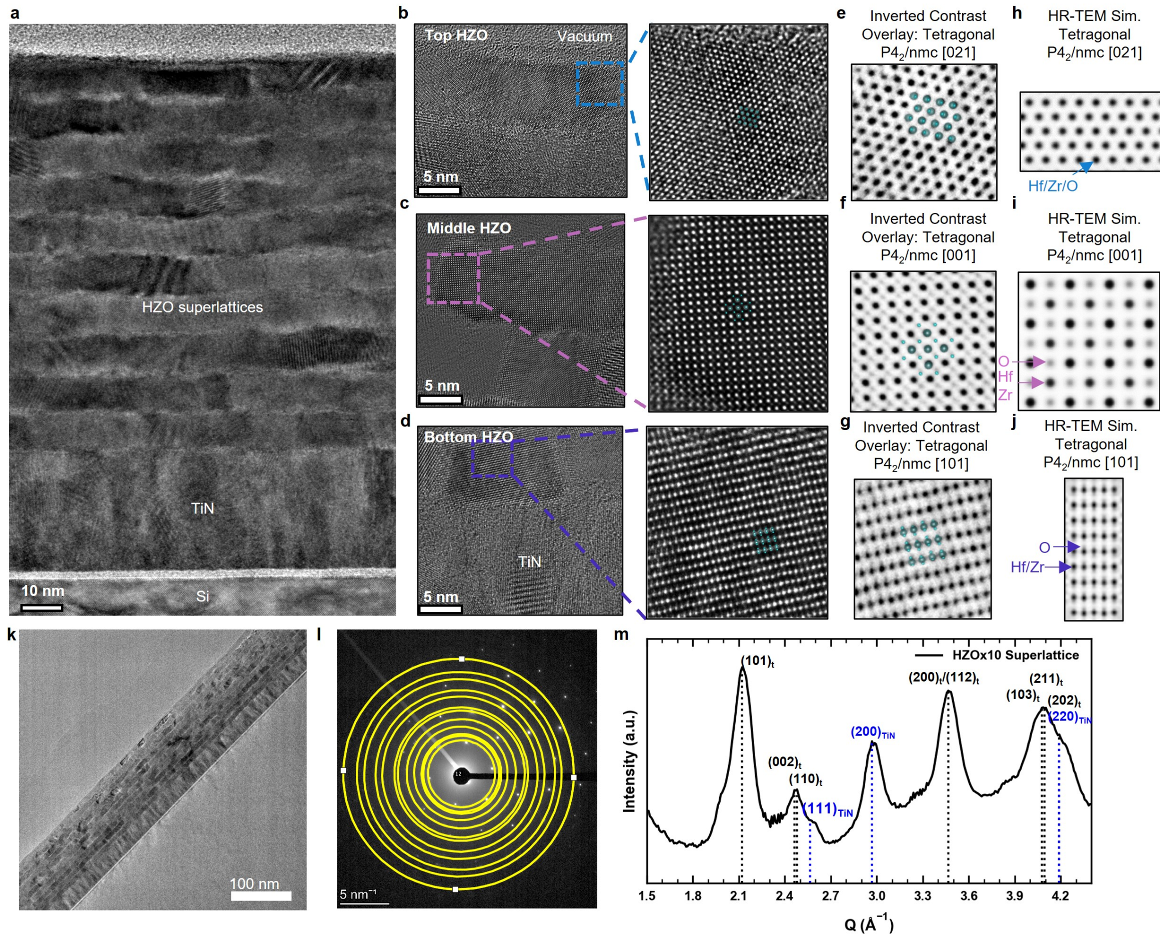

951

952 **Extended Data Fig. 4. Ferroic phase identification in HZOx10 superlattice.** **(a)** Cross-
953 sectional HR-TEM image for the HZOx10 superlattice demonstrating separated Al_2O_3 and HZO
954 layers. **(b, c, d)** HR-TEM (left) and zoom-in HR-TEM (right) images for the top (b), middle (c),
955 and bottom HZO (d) layers in the superlattice. **(e-j)** Top (e, h), middle (f, i), and bottom (g, j) HZO
956 layers are indexed to the t-phase by oxygen-sensitive negative spherical aberration, demonstrating
957 that the superlattice approach maintains the t-phase to the 100 nm thickness regime. For inverted
958 contrast images (e, f, g), the light (dark) atoms represent O (Hf, Zr). For the top HZO layer (e,
959 h), the cation atomic arrangements match to the t-phase [021] zone axis. Along this zone axis,
960 the oxygen atoms overlap with the cations, so only the cations can be matched. Presence of the
961 o-phase and m-phase can be ruled out as they do not have a hexagonal-shaped cation arrangement
962 along a zone axis. For the middle (f, i) and bottom HZO layers (g, j), the cation and anion atomic

963 arrangements match to the t-phase [001] and [101] zone axes, respectively. Overall, the structural
964 identification of the t-phase in the superlattice film is consistent with electrical measurements in-
965 dicating antiferroelectric behavior (Fig. 2, Extended Data Fig. 6). **(k-m)** Wide field-of-view TEM
966 (k), selected area diffraction pattern (l), and corresponding radial profile integration of diffraction
967 pattern (m) for the HZOx10 superlattice film, which indexes to the t-phase, consistent with the oxy-
968 gen imaging analysis. Additionally, the HZOx10 superlattice shows similar $d_{101,T}$ lattice spacing
969 as prior work of $\sim$ 9 nm ZrO_2[85], demonstrating that the superlattice approach maintains a similar
970 strain state across the entire thickness.

971

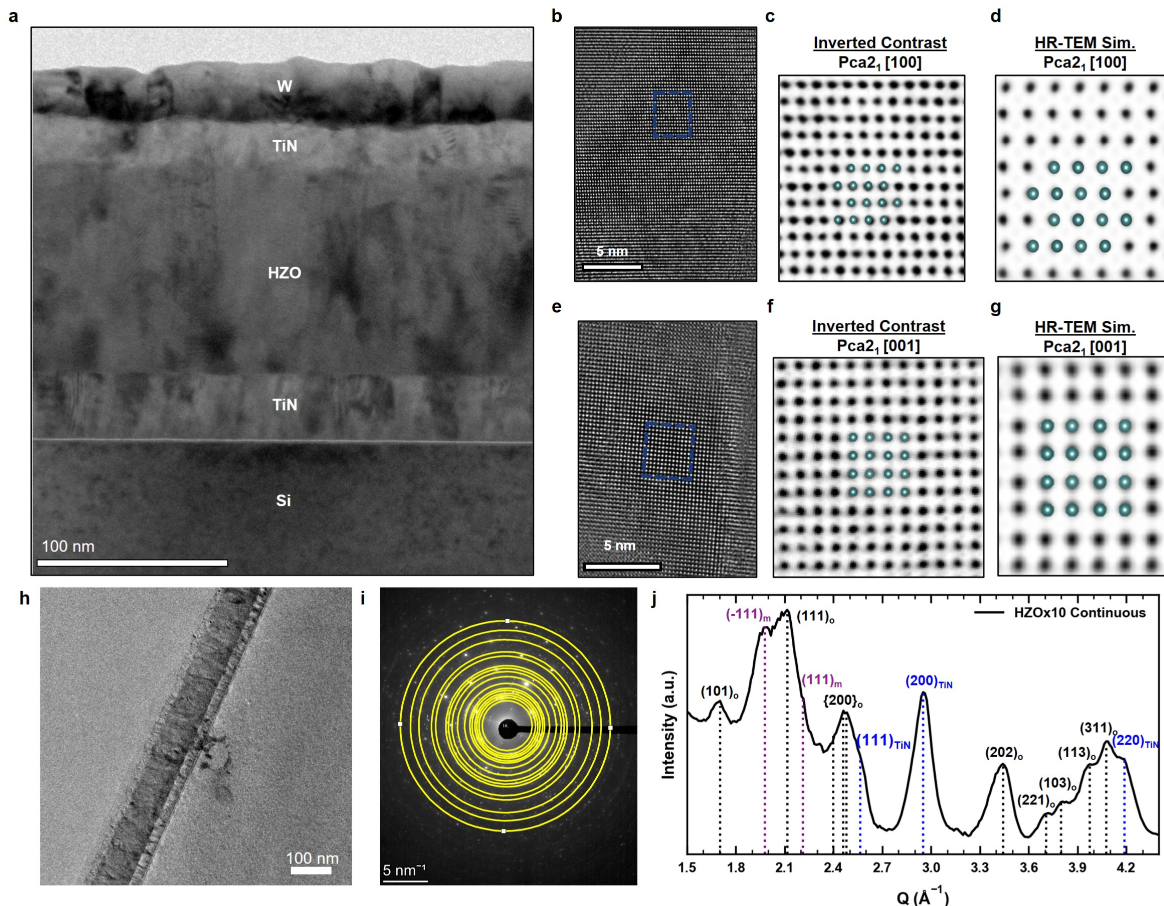

972 **Extended Data Fig. 5. Ferroic phase identification of continuous HZOx10 film from cation**
973 **analysis.** **(a)** Cross-sectional HR-TEM image for the continuous HZOx10 film integrated in an
974 TiN-HZO-TiN MIM capacitor. **(b-g)** HR-TEM imaging of two HZO regions (b, e), inverted con-
975 trast images zoomed-in on single grains (c, f), and corresponding HR-TEM simulations (d, g). The
976 cation arrangement corresponds to the fluorite-structure o-phase ($Pca2_1$) [100] and [001] zone axes
977 for region 1 (b-d) and 2 (e-g), respectively (Supplementary Fig. 9). **(h-j)** Wide field-of-view TEM
978 (h), selected area diffraction pattern (i), and corresponding radial profile integration of diffraction
979 pattern (j) for the HZOx10 continuous film, which primarily indexes to the o-phase, consistent
980 with the cation analysis. The HZOx10 continuous film also shows the presence of some m-phase,
981 which is consistent with the expected phase evolution with increasing thickness[19]. Additionally,
982 the continuous $\sim$ 100 nm HZO film demonstrates similar $d_{111,O}$ lattice spacing as bulk o-phase

ZrO_2[86], suggesting the presence of minimal strain contributions from small size effects. ~~(h-o) Cation sublattice imaging rules out the presence of the fluorite-structure m-phase ($P2_1/c$) in the continuous HZOx10 film upon comparison of the crystal structure projections for the o-phase (h-k) and m-phase (l-o). The [100] and [001] zone axes of the o-phase match the HR-TEM images for region 1 and 2, respectively.~~ Overall, the structural identification of the o-phase in the continuous thick HZO film is consistent with electrical measurements indicating ferroelectric behavior (Fig. 2, Extended Data Fig. 6).

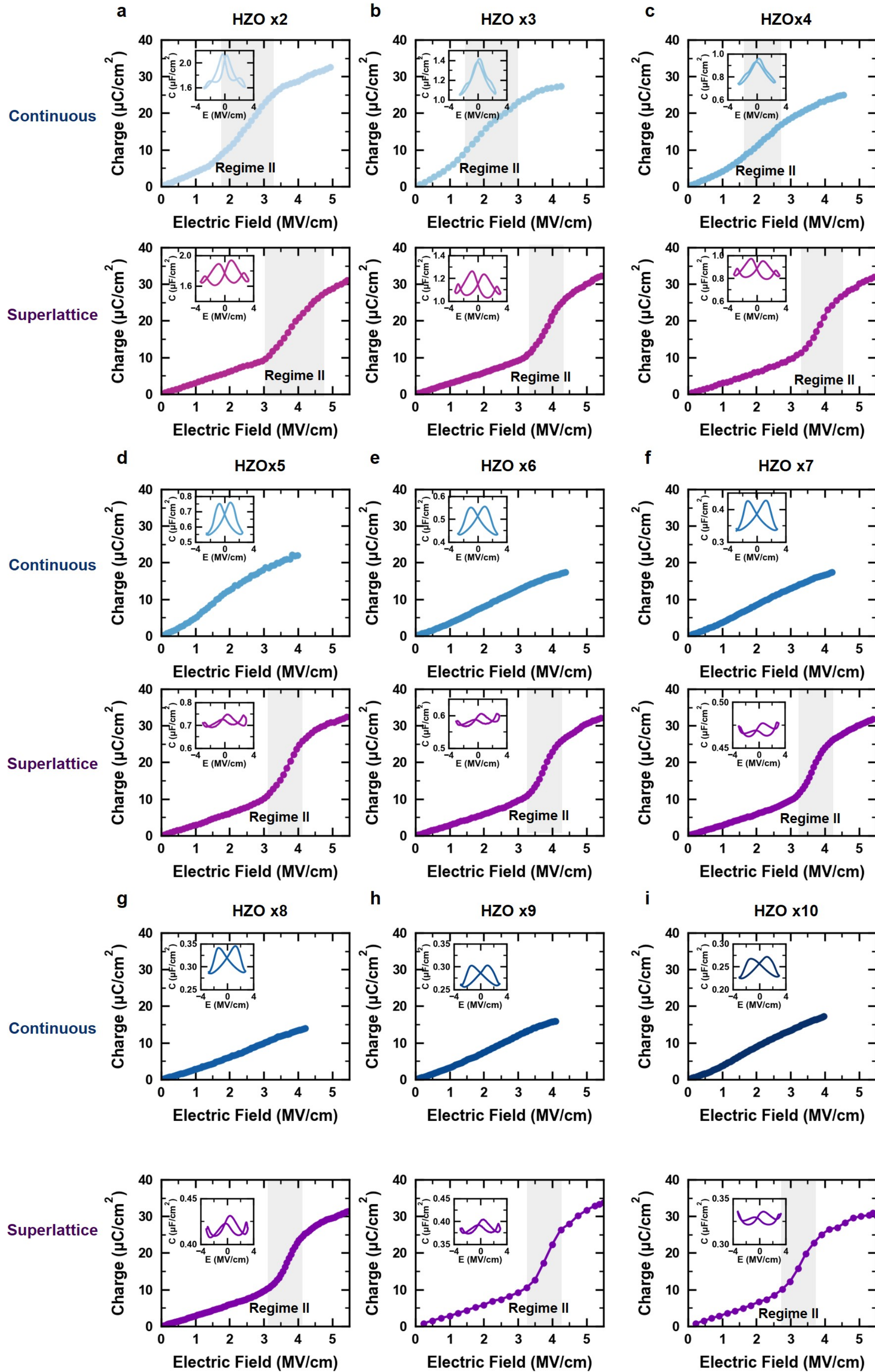

990

Extended Data Fig. 6. Thickness-dependent evolution of ferroic behavior for continuous and superlattice HZO films **(a-i)** Pulsed *Q-E* behavior for both continuous (top) and superlattice (bottom) HZO thickness series to the 100 nm thickness regime. Inset: corresponding *C-V* loops. For the continuous HZO thickness series, an antiferroelectric (HZOx2, a) to mixed antiferroelectric-ferroelectric (HZOx3-4, b,c) to ferroelectric (HZOx5-10, d-i) is observed from the pulsed *Q-E* curve as regime II (and III) eventually disappear for the HZOx5-10 samples, corresponding to the loss of an antiferroelectric-to-ferroelectric field-dependent phase transition. This is additionally confirmed by the emergence of ferroelectric-like hysteresis in the *C-V* characteristics. Meanwhile, for the superlattice HZO thickness series, the antiferroelectric behavior is maintained throughout, as regimes I-III are present for each thickness and antiferroelectric-like *C-V* characteristics are observed. This confirms the ultrathin Al_2O_3 interlayers reset the HZO grain growth ad maintains the desired antiferroelectric behavior. For all figures, the enhanced slope in Regime II is highlighted in gray.

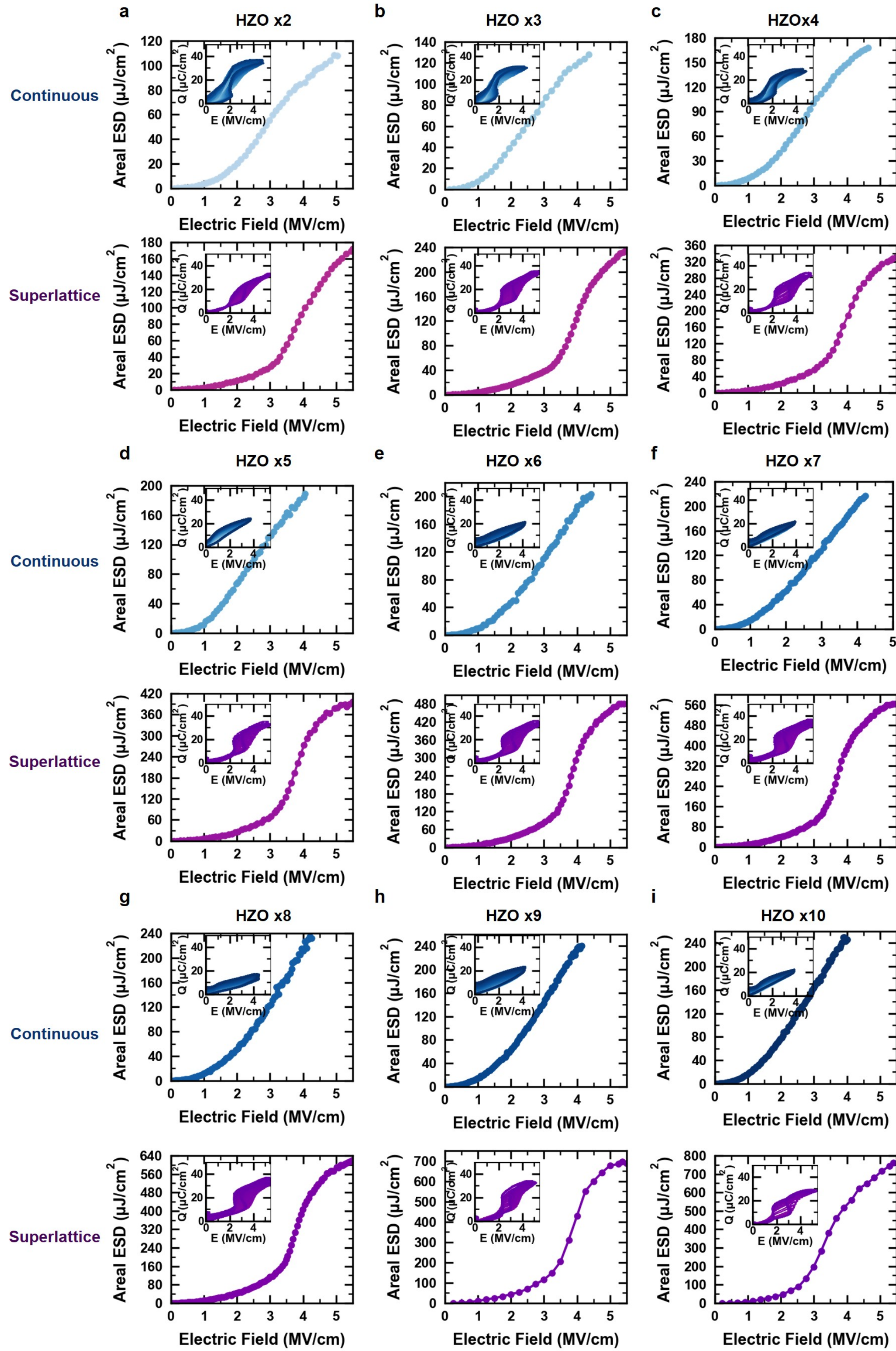

1004

1005 **Extended Data Fig. 7. Thickness-dependent energy storage density evolution** **(a-i)** Thickness-
1006 dependent areal ESD versus electric field for both continuous (top) and superlattice (bottom) thick-
1007 ness series, extracted from hysteretic charge-field measurements (insets). For the continuous HZO
1008 thickness series, ESD saturates with increasing thickness ($\sim 250\ \mu$J/cm^2) as the continuous HZO
1009 films become fully ferroelectric with increasing thickness (Extended Data Fig. 6). Meanwhile for
1010 the superlattice HZO thickness series, the areal ESD scales approximately linearly with thickness
1011 due to the persistence of the desired antiferroelectric behavior (Extended Data Fig. 6).

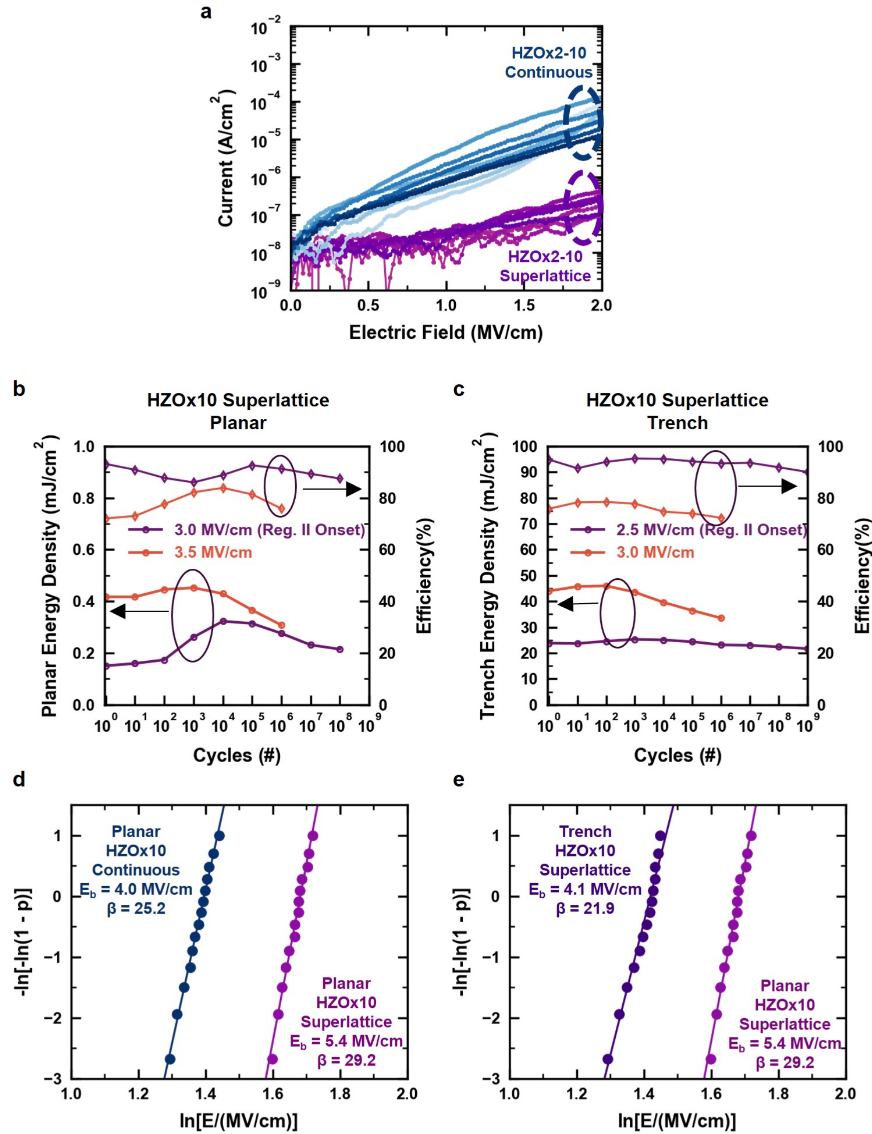

1012

1013 **Extended Data Fig. 8. Reliability characterization** **(a)** Leakage current versus electric field
1014 for continuous (blue) and superlattice (purple) HZO thickness series films. For all thicknesses, the
1015 superlattice approach shows 2-3 orders of magnitude of lower leakage current, derived from the
1016 presence of the high-bandgap Al_2O_3 interlayer and increased number of interfaces. **(b, c)** Energy
1017 storage and efficiency for 2D planar (b) and 3D trench (c) capacitors integrating the HZOx10
1018 superlattice after cycling at two electric fields (1 μs pulses): one near the onset of Regime II (3.0
1019 MV/cm and 2.5 MV/cm for planar and trench, respectively) and another at 0.5 MV/cm higher

field. Near the onset of Regime II, the endurance of both planar and trench capacitors show endurance larger than 10^8 cycles. At 0.5 MV/cm higher electric field, the endurance is beyond 10^6 cycles. ~~after 2.5 MV/cm cycling (1 μs pulses). Both samples survive to 10^9 cycles.~~ **(d, e)** Weibull distribution of the breakdown field, comparing the HZOx10 continuous and HZOx10 superlattice films in 2D planar capacitors (d) and the HZOx10 superlattice films integrated into 2D planar and 3D trench capacitors (e). The 3D trench capacitors shows a 24% lower breakdown field compared to the 2D planar capacitors, likely derived from surface inhomogeneities, which lead to an uneven distribution of electric fields.

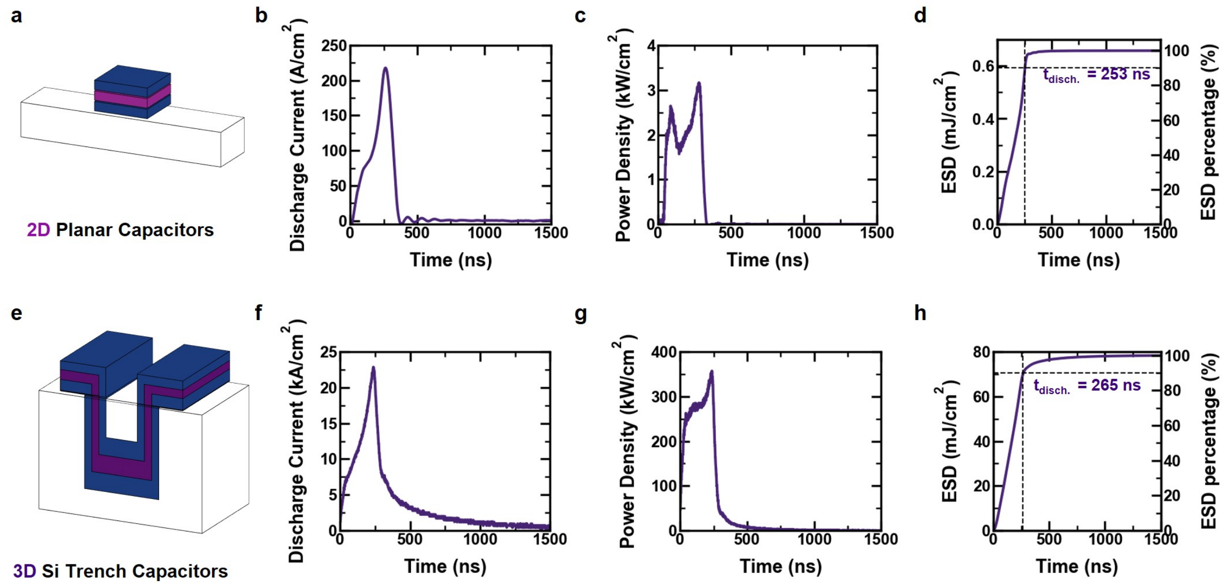

1028

1029 **Extended Data Fig. 9. Power Density Extraction** **(a, e)** Schematic of 2D (a) and 3D trench
1030 (e) capacitor structures. **(b, f)** Measured discharged current versus time during 200 ns fall time
1031 of voltage pulse for both 2D planar (f) and 3D trench (f) capacitors. **(c, g)** Power density as a
1032 function of time for both 2D (c) and 3D (g) capacitors. The power was calculated by multiplying
1033 the measured voltage and current during the discharging stage of the voltage pulse (Methods). **(d,**
1034 **h)** Energy storage density as a function of time for for both 2D (d) and 3D (h) capacitors. The
1035 characteristic discharging time was taken to be when 90% of the stored energy had discharged
1036 (Methods).

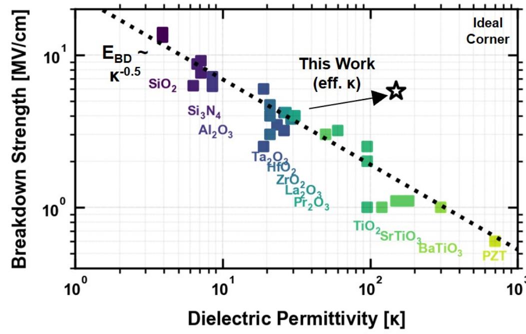

1037

1038 **Extended Data Fig. 10. Permittivity breakdown trade-off** Permittivity-breakdown strength
1039 (κ-E$_{BD}$) relationship for various dielectric materials, which tend to follow an empirical κ-E$_{BD}$
1040 trend of E$_{BD}$ $\sim$ $\kappa^{-0.5}$ [21]. In this work, we engineer the field-induced nonpolar-to-polar phase
1041 transition and its associated NC effect to enhances permittivity during the charging-discharging
1042 process (the maximum permittivity extracted from pulsed *I*-*V* measurements during Regime II is
1043 reported). This approach enables us to overcome the conventional κ-E$_{BD}$ trend which limits energy
1044 storage in dielectric capacitors (Supplementary Text), ultimately leading to the largest volumetric
1045 ESD value reported for a BEOL-compatible dielectric (Supplementary Table 1).